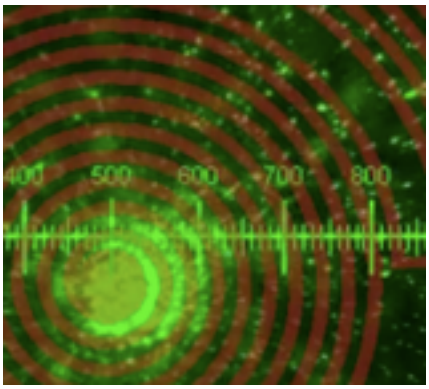

Magnetic traps for bio analyte concentration

Miguel Amaral
Integrated Master's Degree in Physical Engineering
Department of Physics and Astronomy
2016

Supervisor
João Pedro Araújo, Auxiliary Professor, Faculty of Sciences,
University of Porto

Co-supervisor
Paulo Freitas, Deputy Director General,
International Iberian Nanotechnology Laboratory

Microsystems & Nanotechnologies INESC MN

INL INTERNATIONAL IBERIAN NANOTECHNOLOGY LABORATORY

U.PORTO FACULDADE DE CIÊNCIAS UNIVERSIDADE DO PORTO

All corrections determined by the jury, and only those, were incorporated.

The President of the Jury,

Porto, _____/_____/_____

Magnetic traps for bio analyte concentration

Thesis for Physics Engineering Master's Degree

Miguel Amaral

Acknowledgments

I would like to thank my co-coordinator at INESC-MN, Dr. Paulo Freitas, my coordinator at FCUP, Dr. João Pedro Araújo. From the the INL research and technical staff, at the microfluidics lab, I thank Dr. Marina Brito, Dr. Lorena Diéguez, among others; for the fabrication process I thank Dr. João Gaspar and Hélder Fonseca, among others. I thank everybody close to me that helped me getting to this point of my life.

Abstract

This work was inserted in the NANODEM - NANOphotonic DEvice for Multiple therapeutic drug monitoring project, a FP7 European project of which INESC-MN - ”Instituto de Engenharia de Sistemas e Computadores - Microsistemas e Nanotecnologias” is a partner. The project intends to construct a compact device for controlled drug administration. INESC-MN was tasked with constructing magnetic traps for pre-concentration of bio analytes in microfluidics channels. The author contributed to this project via an internship at INL, where INESC-MN was conducting part of the work.

One of the magnetic traps being designed to a NANODEM partner in Germany consists in a 2.5mm*2.5mm *0.3mm volume capable of attraction and repulsion. The design field sources are a permanent magnet and an electromagnet, consisting of 4 planar spiral coils surrounding a central one wired in reverse. This trap was redesigned, fabricated, simulated, tested and optimized. To assist these developments , a simulation tool was implemented, capable of real-time 3D graphical interaction for instant feedback on trap design. The simulation helped to optimize the trap and its predictions agreed with the results of experimental tests, which were successful in capturing, holding and repelling magnetic particles.

Keywords: magnetic trapping, micrometric thin film electromagnets, static magnetic field calculation, magnetic micrometric beads, interactive visualization, interactive design, GPU computing

Este trabalho foi inserido no “NANODEM - NANOphotonic DEvice for Multiple ther-

apeutic drug monitoring project", um projeto europeu do qual INESC-MN - "Instituto de Engenharia de Sistemas e Computadores - Microsistemas e Nanotecnologias" faz parte. Este projeto pretende construir um dispositivo compacto para dosagem automática e controlada de medicamentos por via intra-venosa. Ao INESC-MN foi delegada a tarefa de construir armadilhas magnéticas para pré-concentração de bioanalitos em plataformas microfluídicas. O autor contribuiu para este projeto via um estágio no INL, onde o INESC-MN conduziu parte do seu trabalho.

Uma das armadilhas magnéticas desenhada para um parceiro do NANODEM na Alemanha consiste num volume de 2.5mm*2.5mm*0.3mm capaz de atracão e repulsão. As fontes de campo magnético são um íman permanente e um eletromagnete, consistindo de 4 bobinas espirais planares rodeando uma bobina central, conectada em reverso. Esta armadilha foi redesenhada , fabricada, simulada, testada e otimizada. Para suportar estes desenvolvimentos, uma ferramenta de simulação foi implementada, capaz de interação gráfica com desenho dos campos de força 3D da armadilha e resposta em tempo real a alterações de parâmetros de desenho da armadilha. A simulação ajudou a optimizar a armadilha e as suas predições concordaram com os resultados de testes experimentais, que tiveram sucesso em capturar, segurar e repelir partículas magnéticas.

Palavras-chave: armadilhas magnéticas, electromagnetes de filme fino micrométrico, cálculo de campo magnético estático, partículas micrométricas magnéticas, visualização interativa, modelização interativa , computação em placa gráfica

Contents

List of Tables

List of Figures

Acronyms

INL International Iberian Nanotechnology Laboratory[6]. 1, 7, 10, 12, 15, 18, 20, 21, 27, 40

NANODEM NANOphotonic DEvice for Multiple therapeutic drug monitoring[13]. 1, 7, 10, 49

AFM Atomic Force Miscroscopy. x, 22, 23

APS Advanced Plasma System (ICP-based high density plasma). 57, 61, 62

CPU Central Processing Unit. 31, 32

CSV Comma-separated values. 31

DIW De-Ionized Water. 56

DRIE Direct Reactive Ion Etching. 63

DWL Direct Laser Writting. 54

FCUP Faculty of Sciences of the University of Porto. 1

GPU Graphical Processing Unit. 28, 31, 32

GUI Graphical User Interface. 29

HDMS hexamethyldisilazane (adhesion promoter for photoresist). 54

ICP Inductively Coupled Plasma. 56, 57, 61, 62

INESC-MN ”Instituto de Engenharia de Sistemas e Computadores - Microsistemas e Nanotecnologias”[7]. 10–12, 48

RIE Reactive Ion Etching. 57, 61, 62

SSP Single Side Polished. 54

STP Standard Temperature and Pressure. 4

SVG Scallable Vector Format. 31

Glossary

$[f(i,j)]$ the matrix having the entry $f(i,j)$ at row i and column j. ii, 53

$\hat{A}$ versor in the direction of $\vec{A}$. ii, 53

$\vec{a}\alpha\vec{b}$ $\vec{a}$ is colinear with $\vec{b}$. ii, 53

col_j operator that selects the j-th column of a matrix. ii, 53

row_i operator that selects the i-th row of a matrix. ii, 53

cuboid rectangular parallelepiped. 30

1. Introduction

This thesis describes the process of designing, simulating , optimizing, constructing and characterizing magnetic traps in a microfluidics pre-concentration context for future use in biological assays as part of the NANOphotonic DEvice for Multiple therapeutic drug monitoring[13] (NANODEM) European project. The author is a student from Faculty of Sciences of the University of Porto (FCUP), which previously worked for this project via a summer internship at International Iberian Nanotechnology Laboratory[6] (INL). The author learned about the fabrication process of electromagnets required for the traps, and designed an experimental setup for characterization of cooling systems coupled to the electromagnets. This work was extended to the first semester of 2016-2017 as the introductory part of the master thesis, when more bibliographic research was done. In the next two sections of this document we first go through related literature and analyze the physical aspects of magnetic trapping from a theoretical perspective. Experiments with the magnetic trap device were also performed during this semester. In chapter 2 we detail the magnetic field design, the components and the assembly of this device.

The second semester is the focus of the rest of the document, where during a with a near-full time internship at INL, the author was requested to work on new magnetic traps based on previous designs made for a German group part of NANODEM. The temporal sequence of work was designing the new electromagnets (see section §3.2), and then their fabrication, simultaneous with simulation related work, and finally trapping experiments using simulation results for optimization. The fabrication followed closely previous work done at INL , and is documented in section §3.3.

The author's most individual contribution was the creation of a simulation software providing real-time graphical feedback on particles trajectories under the pull of configurable field sources (chapter 4). From this endeavor resulted improvements to the trap construction parameters. The author also extended the cooling characterization setup and adapted it to the trapping experiments, which are detailed in chapter 5.

1.1. Literature Review

Magnetic trapping consists in the use of magnetic fields for manipulating physical bodies. The potential energy E associated with a punctual magnetic dipole of moment $\vec{m}$ subject to a field $\vec{B}$ is $-\vec{m} \cdot \vec{B}$. In microfluidics applications, the bodies are usually clusters of superparamagnetic nano particles of ferrite. These clusters are superparamagnetic themselves. They are coated with a neutral shell, for instance silica, whose external surface can be functionalized. [14]

Specifically, in this thesis we used magnetic nanoparticles, which have a diameter between 0.2 and 0.5 μm. This is orders of magnitude below the spatial variation of the magnetic fields. The smallest dimension for these corresponds to the tracks of an electromagnet, which in this work are at least 10μm wide. Therefore we can treat the particles as punctual magnetic dipoles.

For these superparamagnetic nanoparticles , the magnetic moment $\vec{m} = V \cdot M\left(\left|\vec{B}\right|\right)\hat{B}$, where V is the volume occupied by the particle and M is the uniform magnetization magnitude inside the particle[8]. M normally has a linear region near the origin and then saturates. Consequently, $U = -V \cdot M\left(\left|\vec{B}\right|\right) \cdot \left|\vec{B}\right|$, and particles are attracted to regions with high field magnitude.

Two field sources commonly used are permanent magnets and electromagnets, the magnets being usually the source of uniform macro fields and the electromagnets of sub millimeter variations in the potential field, although patterned magnetic surfaces

have also been manufactured for trapping purposes [12] . Dynamic traps can be implemented via electrical control of electromagnets or mechanical movement of sources, either permanent magnets or electromagnets .

Magnetized particles emit their own magnetic field, which leads to interparticle magnetic forces. Since the field features are much larger than the particles dimensions, magnetic forces arrange particles in free space as chains that follow magnetic field lines[1, 10, 15].

1.2. Theoretical analysis

The main objective is predicting the trajectory described by particles under the trap influence, therefore first we go through the forces applied to each particle.

The magnetic field generated by field sources applies a magnetic force to these particles which can be obtained from the potential energy: $\vec{F_m} = -\nabla U$.

After some manipulation we obtain:

$$\vec{F_m} = V \cdot \nabla \vec{B} \cdot \vec{B} \left(M' \left(\left| \vec{B} \right| \right) + \frac{M \left(\left| \vec{B} \right| \right)}{\left| \vec{B} \right|} \right) \tag{1.1}$$

Where $\nabla \vec{A} := [\partial_j A_i]$. For more detail see section §B.1.

M and $V = 4\pi \frac{r^3}{3}$ are known, see section 2.2. Our field sources are a permanent magnet and an electromagnet, which is run with constant current for seconds when turned on. Therefore the field can be treated as static. This allows to obtain the field by summing the contributions of each source as if it was isolated. For the cuboid magnet, an article provided the necessary derivation of a closed-form expression[17]. For the electromagnet, the Bio Savart law allows one to obtain the

field by integration over the volume of the current carrying elements of the electromagnet, provided the current distribution is known:

$$\vec{B}(\vec{r}) = \frac{\mu_0}{4\pi} \iiint_C \frac{\vec{J}dV \times \vec{r'}}{|\vec{r'}|^3}, \vec{r'} = \vec{r} - \vec{r_V} \tag{1.2}$$

Where C stands for the volume occupied by the conductor.

For the following calculations we will use for the magnitude of the magnetic force an order of 10^{-14}N. This will be proved to be correct later.

The liquid medium where they move is at rest; the relative speed is the speed of the particle, which we know from past experiments to be below 1mm/s. The fluid is water, at Standard Temperature and Pressure (STP) conditions, so its kinematic viscosity is known. The particle Reynolds number can then be calculated (see table 1.1) using as characteristic length the particle diameter, and turns out to be well below the threshold for laminar flow[19].

name	formula	value	units
fluid density	ρ	1	kg/m^3
dynamic viscosity	μ	$8.9 \cdot 10^{-4}$	kg/(m.s)
kinematic viscosity	$\nu = \frac{\rho}{\mu}$	$8.9 \cdot 10^{-4}$	m^2/s
characteristic length	L	0.3	μm
Reynolds number	Re $= \frac{vL}{\nu}$	$3.4 \cdot 10^{-7}$	-

Table 1.1.: Particle Reynolds number calculation

Therefore we can use Stokes's law to determine the drag force: $\vec{F_s} = -6\pi\mu R\vec{v}$, where R is the radius of the particle, μ is the dynamic viscosity of the fluid and $\vec{v}$ is its velocity.

There is also the gravitic force, which is of the order of 10^{-16}N . The magnetic forces are orders of magnitude above, so we will ignore it.

When suspended in the fluid, that is, not in contact with any surface and far away from other particles, the only forces acting on the particle are the magnetic force and the drag force. Assuming the magnetic force stays constant, we solve for velocity and obtain:

$$\vec{v} = \vec{v_0}e^{-t/\tau} + \vec{v_t}(1 - e^{-t/\tau})$$

where $\vec{v_0}$ is the initial velocity, the relaxation time $\tau = \frac{m}{6\pi\mu R}$ is of the order of the nanosecond and the terminal velocity

$$\vec{v_t} = \frac{\vec{F_m}}{6\pi\mu R} \tag{1.3}$$

is of the order of the μm. With this relaxation time, particles move less than a nm until they attain terminal velocity; for practical effects we can consider that their velocity is the terminal velocity at all times. We can also read each streamline for a magnetic force field plot as a particle trajectory, since $\vec{F_m}\alpha\vec{v_t}$. This analysis agrees with others , with a varying level of detail[20]. However, the surface functionalization of the particles might introduce significant deviations[9].

In our designs particles are pulled against the channel walls, and from past experience we know they they often stay stuck to surfaces. Therefore it would be of interest to study and simulate the interaction of particles and the surfaces of the channel.

Additionally, if the particle concentration is high enough, or the trap concentrates particles in small region, we have observed that these form chains and agglomerate. Other form of interparticle interaction is repulsion once the electromagnet field is turned off. These phenomena might be explained by magnetic forces between particles, and/or electrostatic forces once contact has been achieved.

The magnetic field produced by a sphere of uniform magnetization is the same as

the field produced by punctual magnetic dipole with the same magnetic moment. Therefore equation (1.1) can be reused as long as the magnetic field includes the contribution of all particles except for the one for which we are calculating the magnetic force:

$$\vec{F_i} = \vec{F_m} \left(\sum_{sources\, s} \vec{B_s} + \sum_{\substack{particles\, j \\ i \neq j}} \vec{B_j} \right)$$

.

2. Magnetic trap design

The device previously constructed for a German partner of the NANODEM project is the starting point for the new designs described in this thesis. This design incorporated a permanent magnet and an electromagnet on a chip, under a microfluidics channel of millimetric dimensions, and a cooling system, to balance heat produced by the electromagnet and maintain the microfluidics content in an acceptable temperature range, of the ambient temperature and 5K above. This temperature range limits the power and therefore the current that can be applied to a given electromagnet; in general the current had to be below 1A. Their requirements carried over: a magnetic trap capable of concentrating all particles near a surface region centered in the bottom of the channel, and subsequently repelling them away from that region. The field design that achieves this is detailed in section §2.1.The changes effectively made to the this design were limited to the electromagnet shape and the distances between components, and targeted increasing the effectiveness of the trap. The assembly of these components was constrained by the testing setup of the traps at INL, and the need to vary construction parameters while performing experiments, in order to easily determine optimal values. In section §2.2 we detail each of these components and the magnetic particles used in the experimental tests. Photos of the device in an experimental setup can be found further ahead in figure 5.2.

2.1. Field Design

By vertical order, the channel is above an electromagnet, which in turn is above a permanent magnet. The magnet is uniformly magnetized in the vertical direction, and the electromagnet also generates its largest component in the vertical direction. This ensures that the electromagnet has the best chance to drastically change the norm of the magnetic field when turned on. This creates a new zone of local energy minimums, corresponding to where the magnet and electromagnet fields have the same direction, to where particles migrate. If the current is inverted, these local minimums become local maximums, and particles are repelled from these zones. This can be found schematized in figure 2.1. The distance between the magnet and the electromagnet, between the electromagnet and the channel are critical parameters that determine the field shape and intensity. From previous experiments we knew that they were respectively of the order of centimeters and one millimeter. The channel height also determines the bounds of free movement for the magnetic particles and is therefore equally important. The values used in the experimental tests were chosen by experiment and simulation, detailed further ahead. These were $9mm$ for the magnet-electromagnet separation and roughly $200\mu m$ for the electromagnet-channel separation. The channel height was not varied from its initial value of roughly $200\mu m$ since by experimental observation most particles did not interact with the ceiling of the channel.

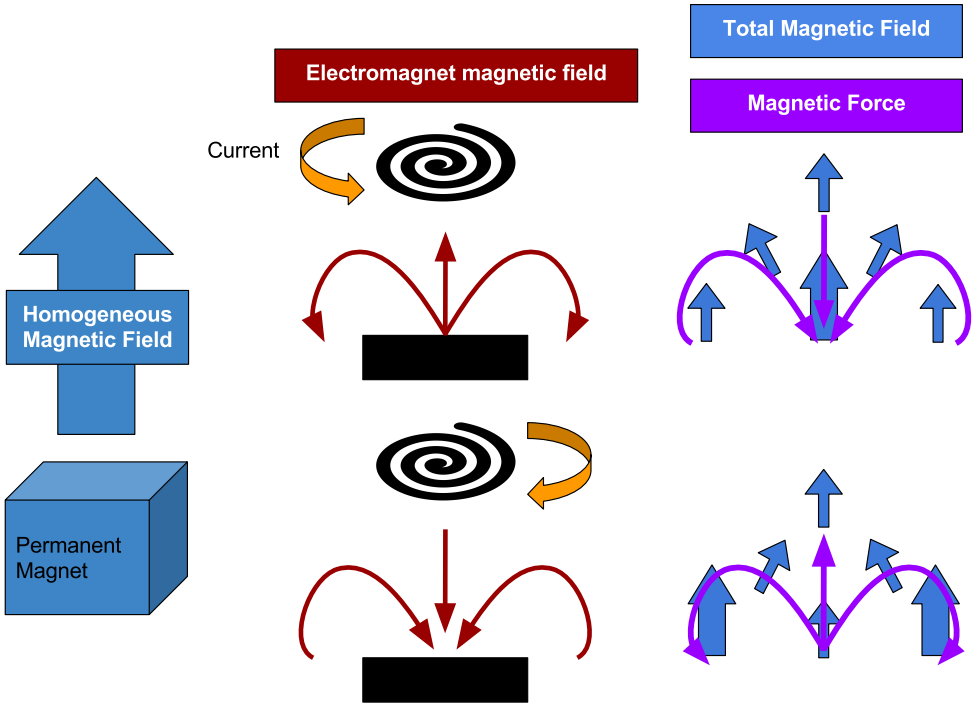

Figure 2.1.: Diagrams for the magnetic field and magnetic force in the studied design, using a single coil as an example of an electromagnet. The arrows schematize the field in a section above and along the diameter of the coil.

2.2. Components

Device Components

Microfluidics Channel

The microfluidics channel was implemented in different ways. Initially, for the German group, the channel was designed to be built using the top of a planarized electromagnet as bottom of the channel. A lid made of cut cover glass was placed on top, separated by two strips of double sided scotch tape. Liquid was introduced via the edges of the channel, using micro-pipette.

Later, these strips were sandwiched by cover glasses, which have a height of roughly

200μm, and the whole construction was simply placed on top of the electromagnet. The additional separation provided by the bottom cover glass was critical for obtaining the desired force field profile.

In both cases, the microfluidics cross-section was roughly 200μm high, $2.5mm$ wide and the channel was roughly$10mm$ long.

Electromagnet

The electromagnet is fabricated as a chip, containing several traps, at INL. See chapter 3 for a detailed description.

Cooling system

From previous experimental work, it was determined that the electromagnet power consumption was high enough to overheat the microfluidics content, going over the 5K above ambient temperature constraint, imposed by the final use by NANODEM partner. This system, developed at "Instituto de Engenharia de Sistemas e Computadores - Microsistemas e Nanotecnologias"[7] (INESC-MN), consists in a copper plate, with internal channels through which a cooling fluid flows, pushed by a micropump through a reservoir, where a cooling fan is mounted. The electromagnet base is covered in with thermal paste, as well as the top of the copper plate, and then they are both put in contact.

Figure 2.2.: Cooler before tubing extension. Micropump to the left, reservoir with fan attached in the center, and copper heat exchanger in the right.

Permanent Magnet

The permanent magnet is a commercial one purchased from Super Magnet[21]. It is a cuboid measuring $8.02mm \times 12.02mm \times 2.01mm$, and its magnetization direction goes through the larger face; we use a previously measured value of 1320kA/m as its saturation magnetization.

Particles

The particles used were *Estapor© Small Carboxyl-Modified SuperParamagnetic Microspheres*, a commercial product from Merck Millipore, with a stated diameter of 0.3-0.5μm; we use 0.3 μm in our calculations. These were functionalized with fluorescent BODIPY© 515 probes. The same batch was used for all experiments. Their magnetization was measured at INESC-MN, see figure 2.3.

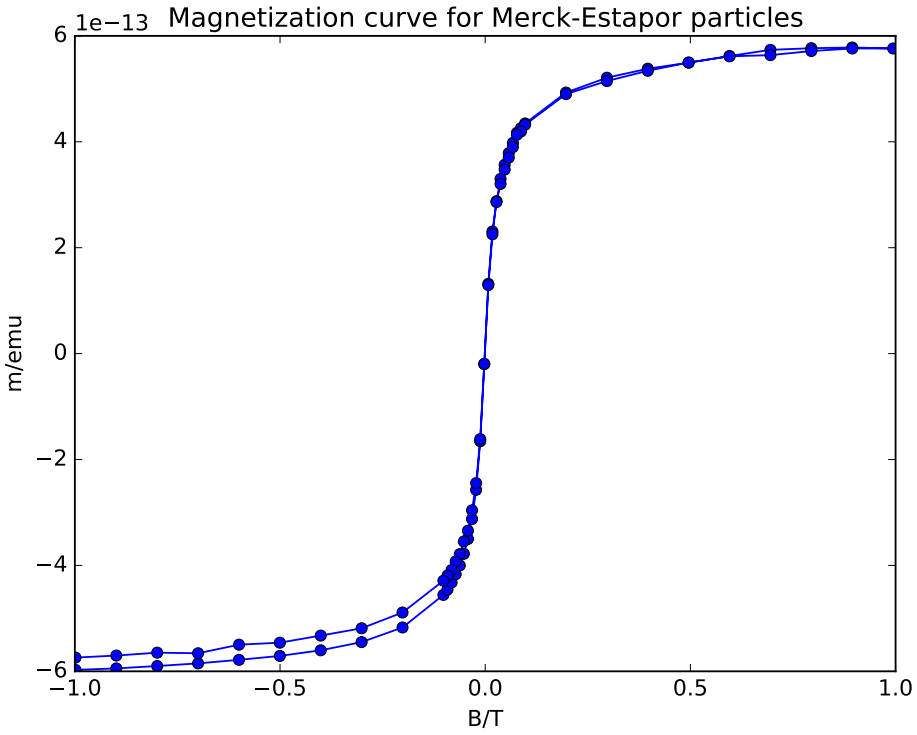

Figure 2.3.: Magnetization curve for particles

From their diameter and measured density at INESC-MN, we estimated the mass per particle, $1.83 \cdot 10^{-2}$picograms.

2.3. Assembly

The testing setup at INL consisted of using fluorescent magnetic nanoparticles, and consequently using fluorescence microscopes, which have limited space for large assemblies. This, together with the small size of some of the components, forbade the use of all purpose holders. The solution was using small stripes of scotch tape to hold components together. Specifically, the channel was lightly taped to the electromagnet, which was held in place mostly by the thermal paste to the cooler plate. The cooler plate was strongly tapped to a microscope slide. This slide was held

in place by the stage tweezers of the microscope. The magnet was placed on top of the microscope condenser, which stage was used to vary its vertical position. This condenser was not in use, since the fluorescence light path came trough the objective. This allowed the variation of the distance between the magnet and the electromagnet. The separation between channel and electromagnet was deemed too difficult to be made variable, obliging to the construction of different channels in order to test different separation values.

A device schematic can be found in figure 2.4.

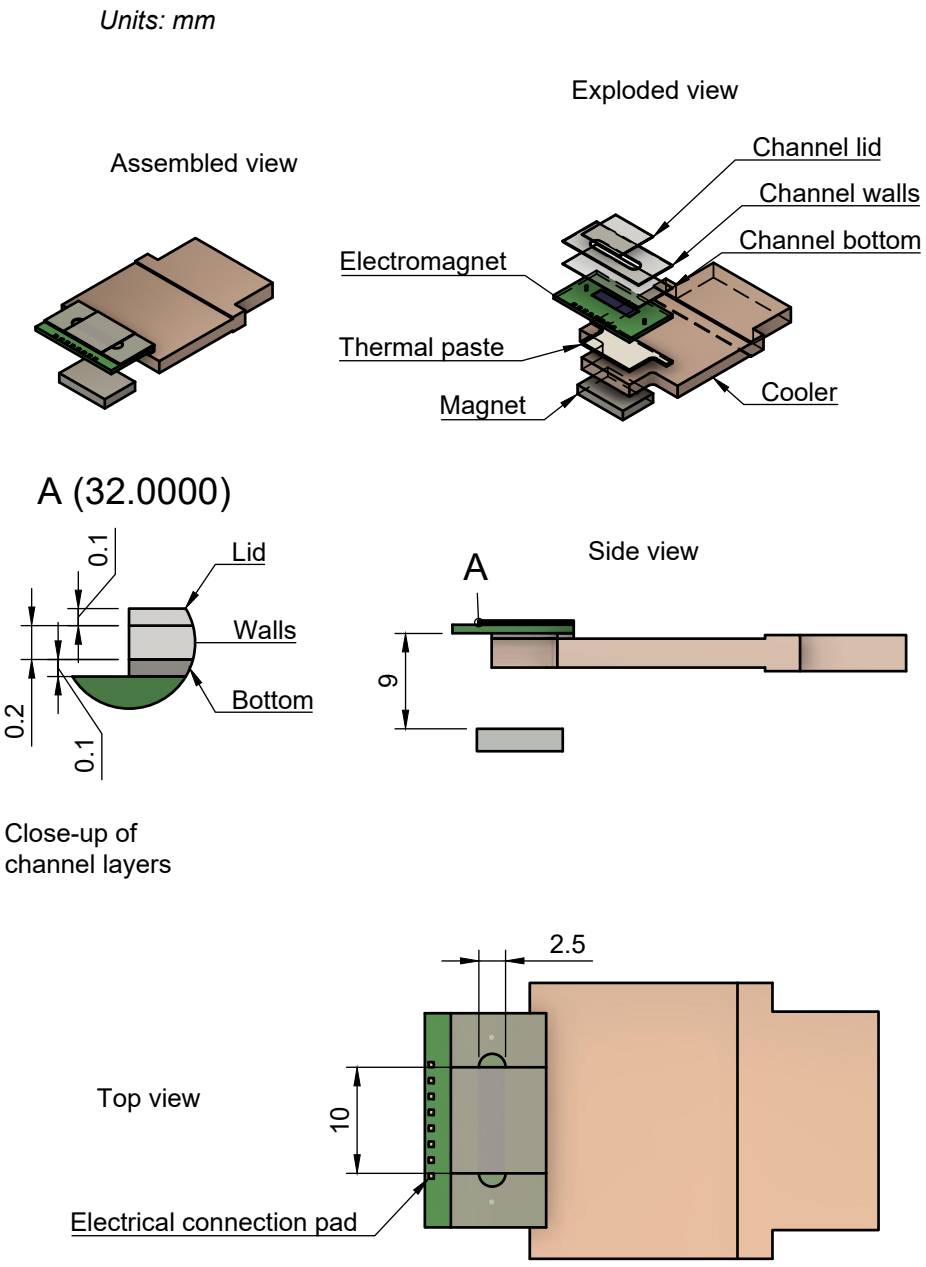

Figure 2.4.: Device schematic

3. Electromagnet design, fabrication and characterization

3.1. Introduction

The electromagnet design inherited from previous research produced at INL consists on a chip of roughly $1cm \times 2cm \times 1mm$, which has 4 separate independently addressable $2.5mm \times 2.5mm$ sections, each containing several electromagnets connected in series. Any of these electromagnets consists of a planar path with a $40\mu m \times 15\mu m$ (roughly) copper cross section, and through which a DC electrical current is passed. These planar paths and the number of electromagnets are what was modified . In each section, these electromagnets are connected in series, with both ends ending in large $50\mu m \times 50\mu m$ copper pads. These connections are done either at the same level using copper tracks of larger width, in order to minimize heating by Joule effect, or underneath the copper via a another metal layer , which is selectively isolated from the above copper tracks.

3.2. Designs

The previously tested design for the German group was what we will term here the “normal” design: a central coil at the center of a rectangle formed by 4 other lateral coils, these last wired in reverse in relation to the first (see figure 3.1a). All coils

have 10 loops, an inner radius of $40\mu m$ and a external radius of $340\mu m$, for a total diameter of $680\mu m$.

The new designs increase the number of loops of the central coil from 10 to 18, resulting in an external diameter of $1160\mu m$, and/or add windings to the current path between the center coil and the others, and/or change the placement of lateral coils from a rectangle to a square. The correspondence between design and designation can be found in the labels of the sub-figures of figure 3.1.

The windings were generated by writing a computer program in the PYTHON programming language that offsets the outline of the lateral coils and an enclosing rectangle, while linearly distancing the the new segments from the originals, and merged the resulting segments into the desired winding. This resulted in a path that weaves in between the lateral and central coils, with 8 side-by-side tracks, each with the same cross-section as in the coils, $40\mu m \times 15\mu m$. The current goes through the windings with the same rotation direction as it goes through the central coil. As a side effect of the program construction, it was possible to vary some parameters. The program initial parameters for the windings generation were varied to yield two different designs, code-named “filling-close”, seen in figure 3.1e, and “filling-large”, seen in figure 3.1f. These designs place the lateral windings respectively closer and further away from the central coil.

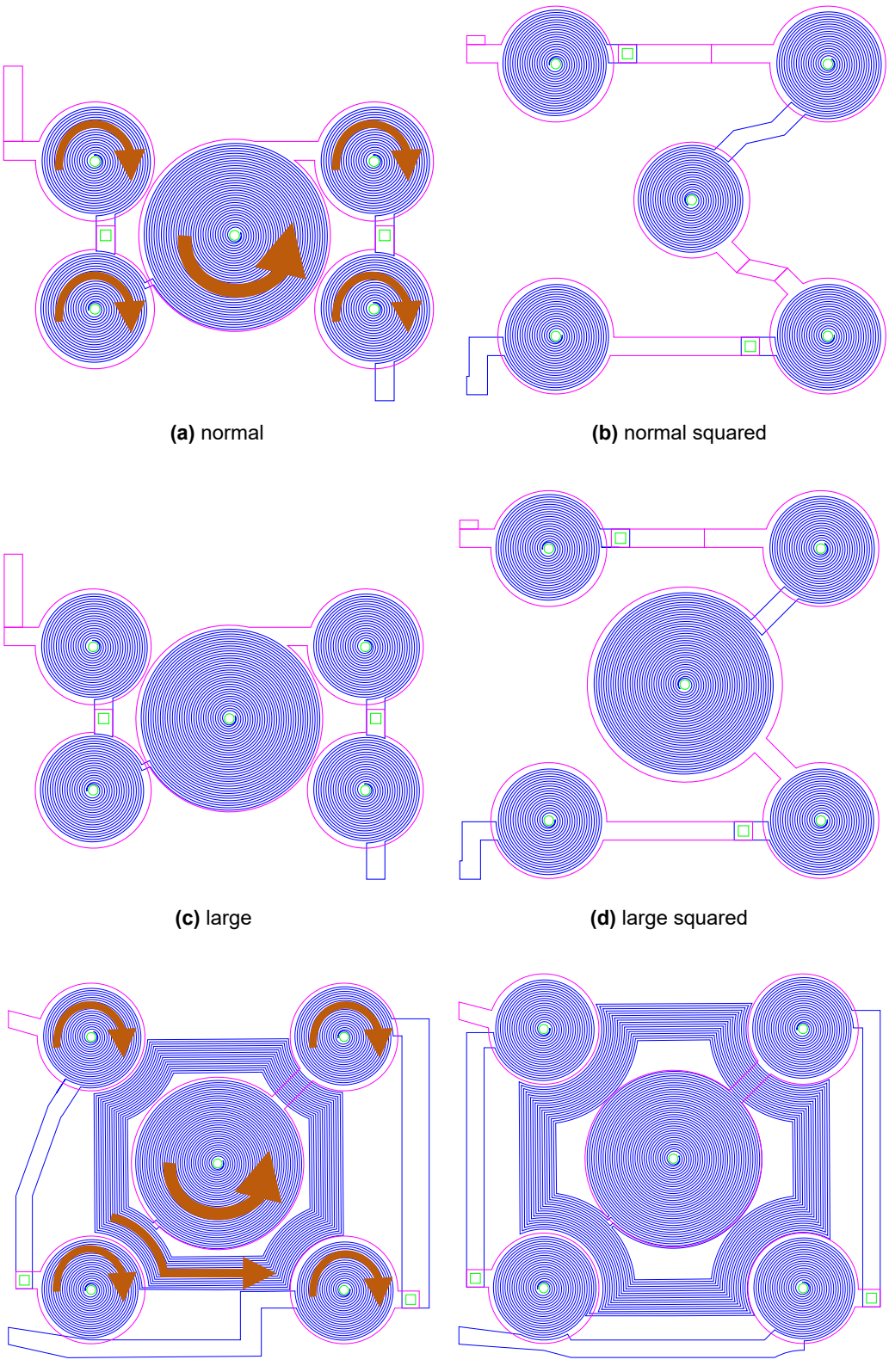

(a) normal

(b) normal squared

(c) large

(d) large squared

(e) filling close

(f) filling large

Figure 3.1.: Fabrication masks for each design type, labelled with their designation, edited so that blue regions correspond to the electromagnet tracks. The full mask color code can be found in figure 3.2.The orange arrows exemplify the current orientation for two designs, the others follow the same pattern.

3.3. Fabrication

Fabrication was directed by João Gaspar at INL. The author studied and documented the fabrication and moved the substrates from process to process, which were effectuated by the corresponding technicians; most control steps were effectuated by the author. Most processes details were saved as programs in the respective machine's controllers, and were not documented.

The construction consist in a bottom metal layer for routing the current from the pads to the center of the coils, followed by $40\mu m$ high copper tracks forming the electromagnets, a polyamide topography uniformization and finally a reflective coating. Direct writing was not possible for the lithography corresponding to the copper tracks, due to their high height. Hard masks were fabricated not only for this step, but for each required lithography; see figure 3.2 for a legend. The fabrication of theses masks is detailed in section A.1.

color	name
	1:metal
	2:holes
	3:tracks
	4:pads

Figure 3.2.: Masks legend

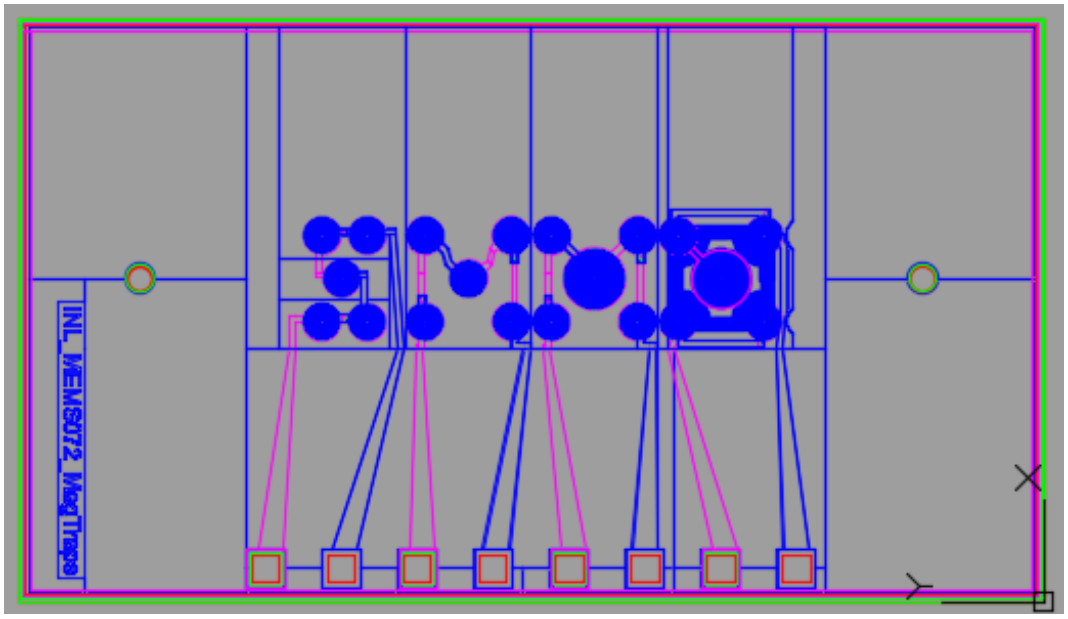

Figure 3.3.: Screenshot of .dwg file showing all masks layers of a mixed set die.Pads for connections at at the bottom; two holes for microfluidics connections are present at left and right.

The different sets were combined into 8 die types. 6 of them consisted in having all sets in a die being of the same type; the other two combined different set types as to cover all set types between each other. The final production run after several attempts resulted in 2 wafers of dies, see figure 3.4 for their placement. The fact that hard masks were used made fabrication time smaller, when considering the multiple attempts and multiple wafers produced.

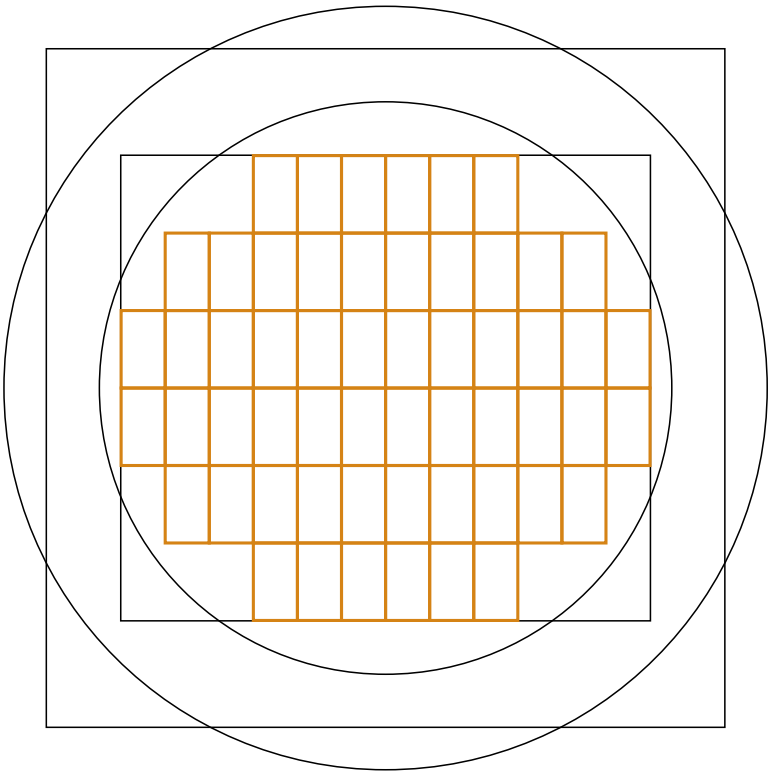

Figure 3.4.: Die placement (smaller rectangles) on wafer. The larger circle corresponds to the wafer limits; the inner black outlines, including the large black rectangle, correspond to constraints imposed by the fabrication steps.

The fabrication steps of the chip are described in A.2, which includes a schematized section of a chip for each stage. The run sheet is highly specific to the INL facilities, and does not contain most processes details, which are saved as programs in the respective machines, and therefore is not included. A cross section running along a single coil similar to the ones fabricated is schematized in figure 3.5.

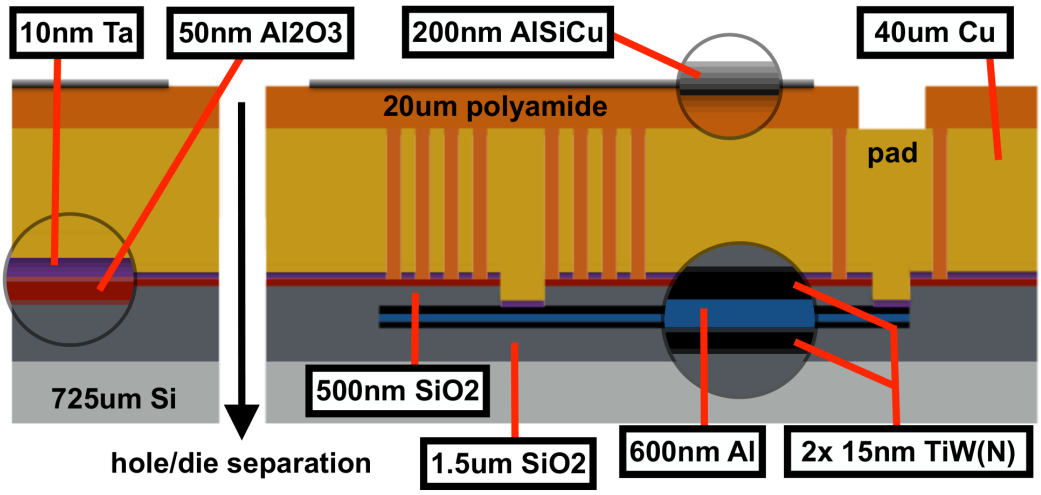

Figure 3.5.: Schematic of the cross-section of a generic coil electromagnet built into the chip (not to scale).

After the chip is fabricated, the electromagnet pads are wired to malleable cables by wire-bonding, effectuated by Marco Martins at INL.

3.4. Characterization

3.4.1. Topography

Using a mechanical profilometer, the actual copper height of the tracks was measured before coating with polyamide. Due to issues with the copper electroplating step, which machine had been stopped for some time, this height varied roughly from 20 to 45μm. See figure 3.6 for a measurement example.

Despite this lack of uniformity, via visual inspection using a microscope the tracks were well defined. The width of the tracks was larger than expected, at roughly $20\mu m$ and the separation between tracks at $10\mu m$.

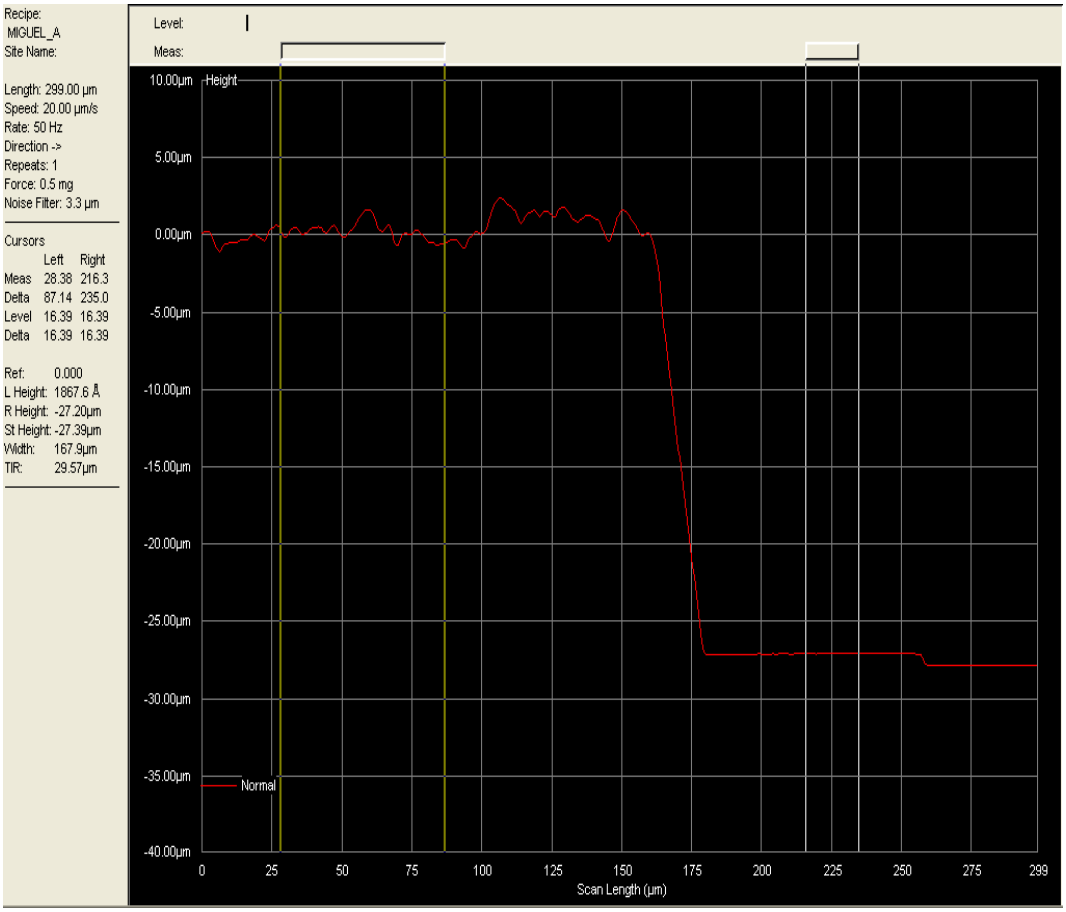

Figure 3.6.: Profilometer screenshot, showing a 25um height between the seed layer and the top surface of copper, after electroplating.This corresponds to the state schematized in figure A.11.

After finishing the fabrication, an Atomic Force Miscroscopy (AFM) measurement, originally meant to measure magnetic field, revealed that the surface still had a height variation of 3μm, where the tracks were located (see figure 3.7).

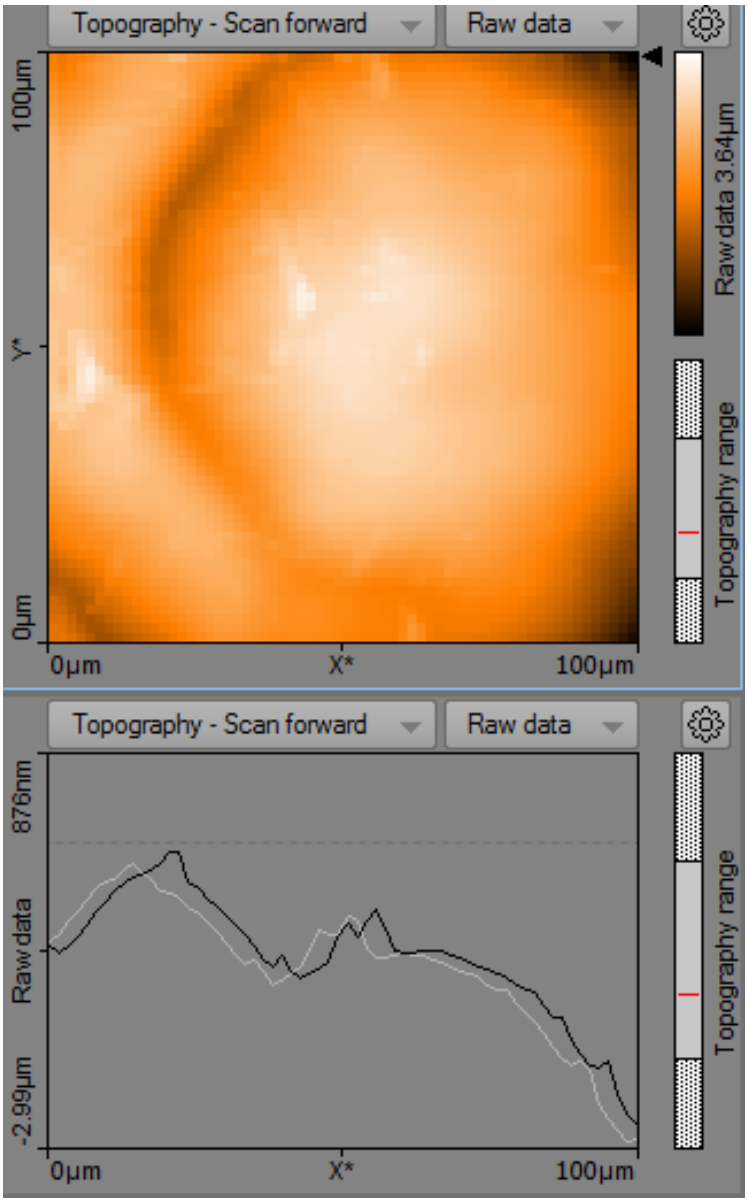

Figure 3.7.: AFM measurement near the center of a coil.

3.4.2. Resistance

Each die was marked with an identification number. For each die, first a 500mA current was passed through each of the 4 electromagnet sets for at least 2 seconds; some seconds after, the resistance between each of the 5 pairs of adjacent pads

was measured with a ohmmeter. The connection to the pads was done manually via multimeter probes. After excluding electromagnet sets with open circuits or short-circuits to other sets, histograms for each of the set types were produced (figure 3.8).

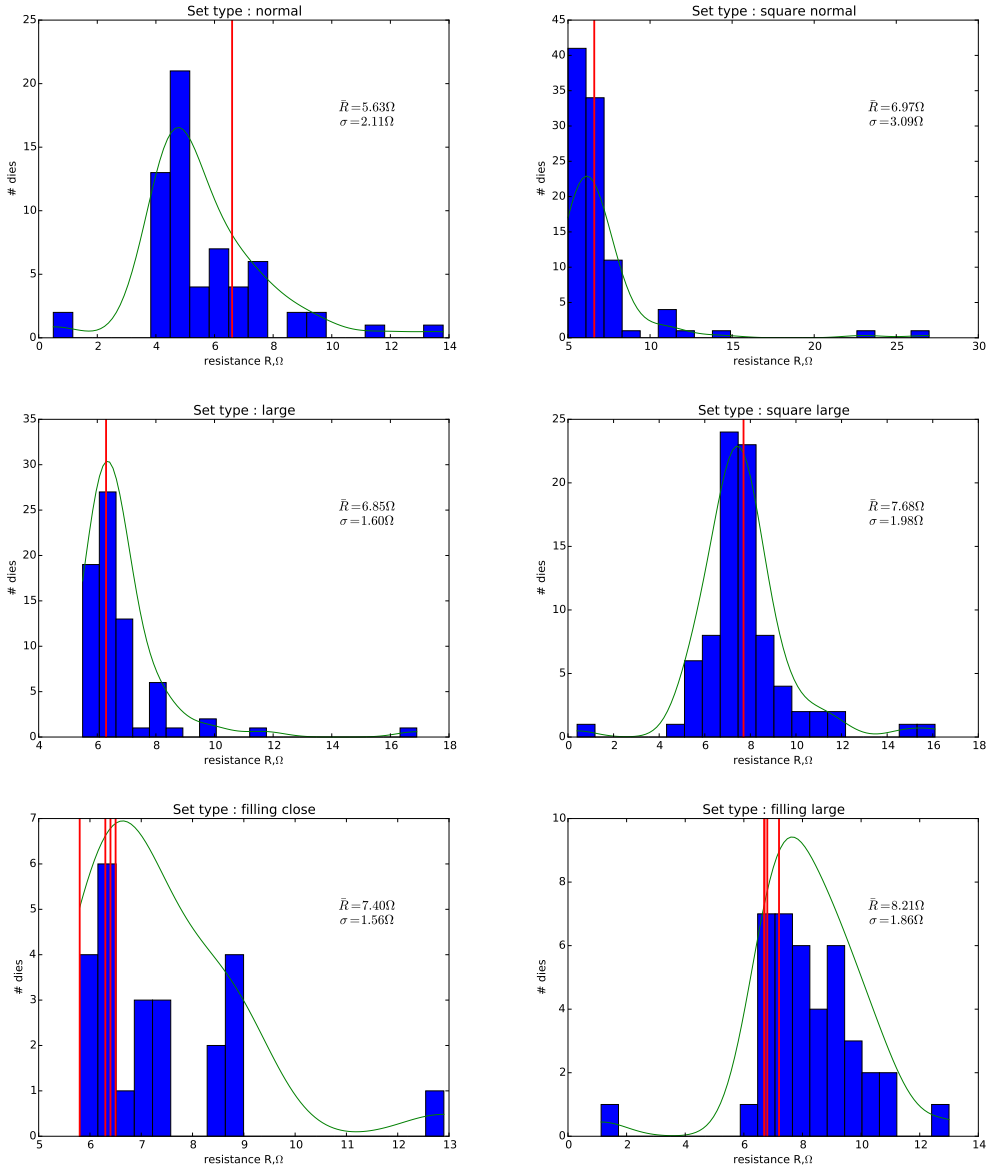

Figure 3.8.: Histograms (blue) of circuit resistance for each set type. Kernel density estimation in green. Values corresponding to chips used in experiments in red. The plot set type matches the naming in figure 3.1.

3.4.3. Cooling

The cooling system was tested by running a sequence of current pulses of 2s each, separated by 4s, with a current between 0.5A and 1A, and registering the circuit resistance temporal evolution. This sequence was chosen for it gave a temperature evolution profile near the acceptable limit for similar past electromagnets. The temperature variation ΔT was estimated by using the formula $\Delta T = \frac{\Delta R}{R_0}\frac{1}{\alpha}$, where $\alpha = 3.9 \cdot 10^{-3} K^{-1}$[5] is the temperature coefficient of the resistivity for copper at 20ºC. The main objective of this analysis is to make sure the temperature does not fluctuate much more than 5ºC, as to not damage biological matter in future applications.

The results for the “filling close” design (see figure 3.1e) in two different configurations are shown in figure 3.9. The first configuration is the one where the top of the chip functions as the bottom of the channel, and is therefore in contact with a liquid. The second configuration consists in using a glass cover as the channel bottom.

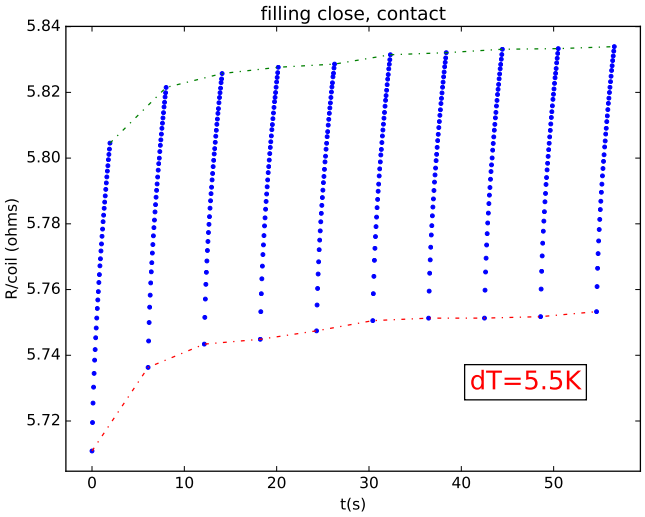

(a)

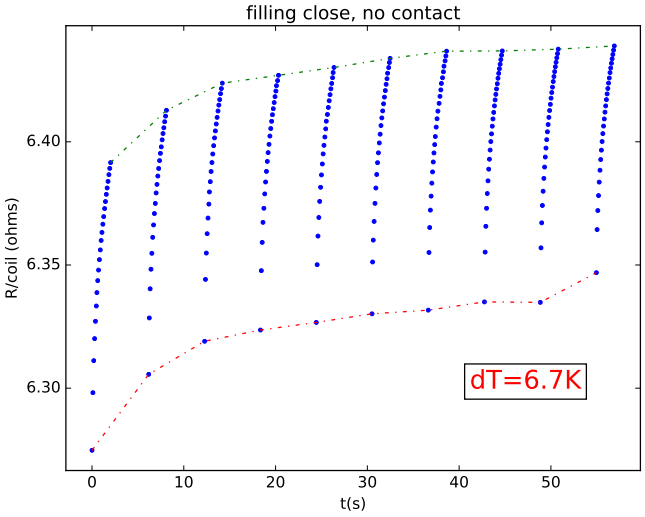

(b)

Figure 3.9.: Cooling results for the “filling close” design, in different configurations. These results were obtained by using a current of 1A. The data points measured are colored blue, and correspond to instants where the electromagnet was turned on; a limitation of the experimental setup resulted in no data capture for offline periods. We note a fast increase of temperature in the first 2 to 3 cycles, followed by a slower slope. The slow increase is not worrying since for at least a minute the temperature remains in an acceptable range, and that time is enough for running the required trapping experiment

4. Simulation

4.1. Introduction

In this section, we first explain the initial motivation behind simulating magnetic trapping. Then we identify the phenomena we might want to study. After reviewing the literature for pre-existing solutions, we establish the goals for our program.

4.1.1. Motivation

The process of fabrication and testing a electromagnet for magnetic trap is time-consuming, in the best of the cases observed by the author at INL taking two weeks and in the worst roughly a month. It is therefore of interest to be able to predict the behavior of such devices.

For simple configurations a hand-written calculation is enough; however, when one wants to be able to generalize and study many possible 3D placements of field sources, or mix local and macro approximations to the field, it is more productive to have a general method that can fitted to specific designs very quickly.

After the electromagnet is fabricated, the the trap must be assembled. The placement of its elements depends on the require behavior of the trap; a simulation can provide a virtual environment where to displace these elements freely until a proper behavior is observed.

4.1.2. Literature review

There are software packages dedicated to the calculation of magnetic fields. These are usually focused on finite elements, where the entire simulation region is parceled into a grid, and boundary conditions determine the field inside. One example is COMSOL MULTIPHYSICS®[4]. This is suitable for complex geometry where the magnetization or current distribution is not known.

In the opposite case, it's simpler to sum the contributions of each field source to obtain the total field. A software package named BIOSAVART[18] using this method a providing a 3D visualization was found; however its interface for field source description and manipulation is text based .

None of the found software provide a graphical user interface to the placement of the field sources while simultaneously giving real-time feedback.

Interparticle interaction is a topic that leads to molecular dynamics. However, the software packages have no easy graphical interface or built-in magnetic field calculators. Forces between particles are modeled by potentials, which results in accurate results; yet, to avoid interpenetration of particles, they use a small time step that renders real-time simulation impossible. One such example is LAMMPS[11]. Physics engines for rigid bodies are pieces of software normally found in game making frameworks. These are designed to simulate Newtonian mechanics of up to 1000 entities, , but they often sacrifice physical accuracy for speed and appearance. Specifically, BULLET PHYSICS[2], a physics engine, can go two orders of magnitude, that is 100k entities, using Graphical Processing Unit (GPU) parallel computing abilities.

Nevertheless, simulating the particles as hard spheres acted upon by magnetic forces results is a reasonable approximation.

4.1.3. Targets

The simulation was to focus on these properties:

- Interactive: the user should be able to modify the design and see in real-time the result of it's actions on the trap functioning, via a Graphical User Interface (GUI).
- 3D visualization of the magnetic field and the resulting force field
- simulation of particle movement, including collision

Additionally, two items of lower priority were studied, but not fully implemented:

- interparticle interaction, namely the magnetic force between magnetic dipoles
- surface-particle interaction.

4.2. Implementation

The software used was the game development software UNITY3D[22], which is scripted in the C#[3] language. This software comes with a graphical editor. The user defines objects, places them in 3D space, and can attach a variety of components to them, such as scripts that enable general behavior. The editor automatically builds GUI's for user-written code. For our purposes, these abilities dispensed with the need to write a GUI for the simulation; we simply used the UNITY3D editor as the interface for the simulation.

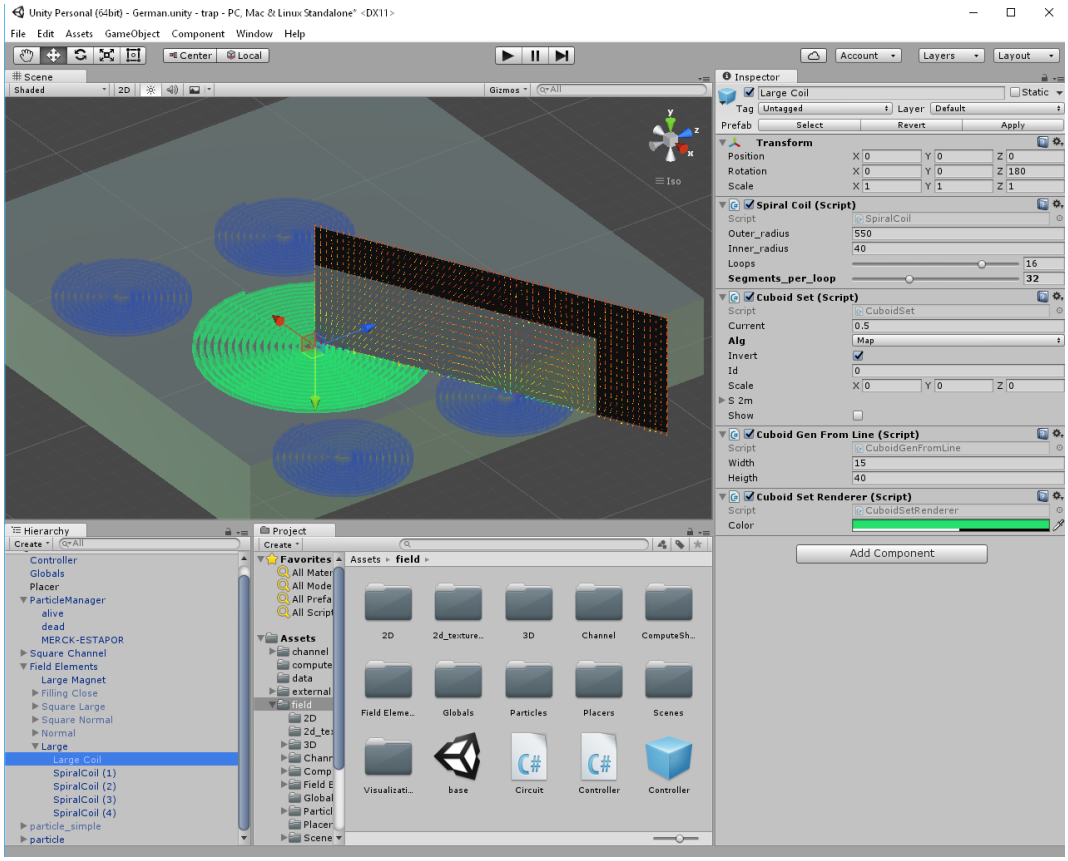

Figure 4.1.: Screenshot of the UNITY3D editor graphical environment. A video can be found here.

The calculation of the magnetic field for electromagnet sources required an integration step. In some cases, this integration can be expressed in close-form, which is much simpler to code and efficient to run. Given the variety of electromagnet designs , some of which are decidedly not easily parametrizable and therefore difficult to reduce to closed-form, we took a mixed approach. Each conductor is approximated by a series of cuboids. Using a closed-form expression, the field contribution for each cuboid is calculated and added to a total. The author provides a derivation of this formula in section §B.2 as well as pseudo-code for its evaluation in section §C.1.

For permanent magnet sources of cuboid shape, there is an easily calculable closed-

form expression, see 1.2.

For each field source, the magnetic field and the gradient of the magnetic field are calculated. Once the total of each is known, the magnetic force is calculated using equation (1.1).

M is accurately represented using a linear combination of 3 scaled Langevin functions, i.e. $M(x) \approx \sum_{i=3}^{3} a_i L(b_i x)$, where $L(x) := \coth(x) - \frac{1}{x}$.

The calculation is equivalent to a sum of closed formulas, therefore the precision of the results is affected by rounding error, the precision of the data types used to represent numerical values, which might change between calculations, and the coarseness of the discrete representations of real-world data. Using cases for which exact formulas exist, the effective precision of the results of magnetic and force fields was determined to be roughly 3 decimal cases. The electromagnets were represented exactly for the straight sections, and the number of cuboid elements used for curved sections was roughly 80/360º.

In the next paragraph , we use the term field interchangeably for either the magnetic field or the magnetic force field.

After some profiling, it was noted that using the Central Processing Unit (CPU) these calculations would take too long to provide an interactive visualization of the field. We concluded that a viable alternative would be using the parallel processing capabilities of the powerful GPU present in the same machine. Parameters and the cuboids list are copied form the CPU to the GPU, where the field calculation and rendering of the visualization takes place. Specifically, the field is rendered in 3D as lines of varying color and size, normalized by field magnitude.

Data can be exported from the simulation into a Comma-separated values (CSV) file. For 2D regions, a PYTHON[16] script reads the data and plots the vector field as streamlines, which can be saved. among other formats, as a Scallable Vector Format (SVG), for publication purposes.

For simulating particle movement, a Newtonian physics engine was required, for

handling collision with the channel walls. This is obligatory, since the force fields quickly pull the particles down, towards either to the electromagnet or the permanent magnet. Ideally we would use the GPU, but physics engines are complicated to code and none were available for the framework in use. Therefore we used the built-in physics engine from UNITY3D. Each simulation step, the position of the particles is sent to the GPU, the force field is calculated at those coordinates, and the results are copied back to the CPU and fed to the physics engine as impulses that guarantee that the particles speed will be as in equation (1.3). This obviously is not correct when the particle is near or in contact with a wall; even so, since the impulse is projected due to the normal force applied by the wall, the particle remains in bounds.

These program components and data flows are illustrated in figure figure 4.2.

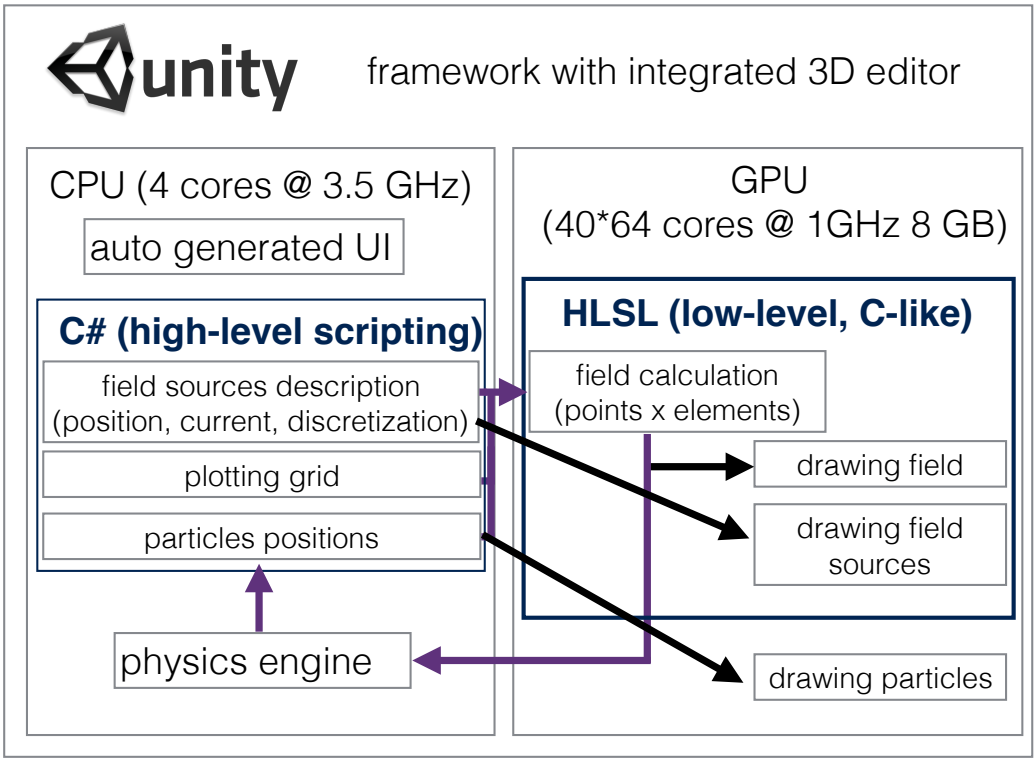

Figure 4.2.: Diagram of the simulation software. Arrows are painted differently for better clarity, nothing else.

4.3. Results

For the following section, we used a 9mm vertical distance between the magnet and the plot region. This value was determined experimentally to be the optimal distance for the trap to function. A vertical distance of $10\mu m$ between the electromagnet and the plot region was set, to emulates the presence of the irregular polyamide layer. These parameters can be better visualized in figure 4.3.

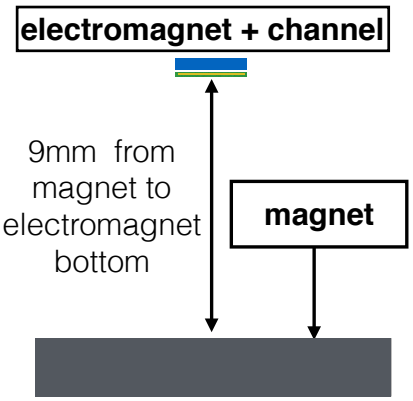

(a) Macro-view of the device showing in scale the relative sizes of the electromagnet and channel in relation to the magnet.

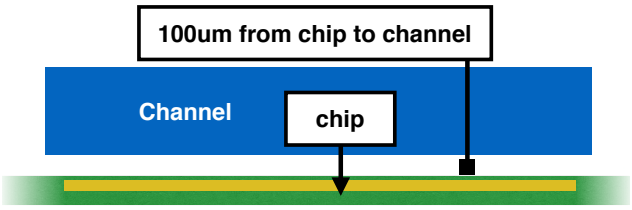

(b) Close-up of the electromagnet and channel in scale.

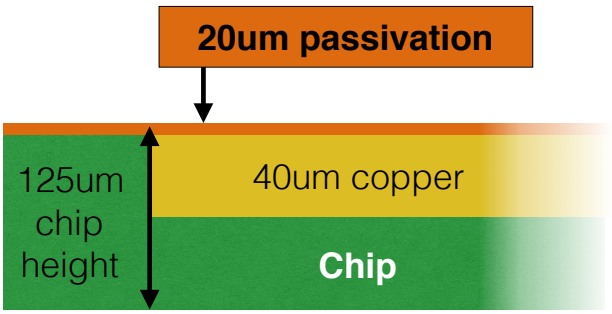

(c) Diagram in scale of the electromagnet chip.

Figure 4.3.: Diagrams for construction parameters used in the simulation

4.3.1. Magnetic Force Field

For each electromagnet design, plots of the magnetic force field were done along several sections. Here we present cuts from the center to a corner (“diagonal”),

and a close-up (“diagonal close up”), focused on the space between the central coil and a lateral one. Additionally, there are different plots for the current value being passed through the electromagnet: 0, 0.5 and -0.5 A. In figure 4.5 plots regarding the “filling close” and “normal” designs can be found (the designations in quotes can be matched to their designs via figure 3.1). In all cases the plotted region is $10\mu m$ above the top of the electromagnet.

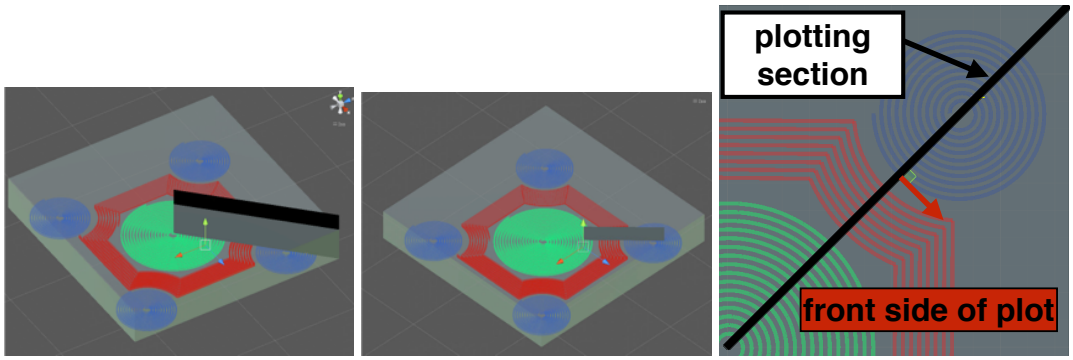

(a) Center to a corner **(b)** Close-up of the “center to a corner” region **(c)** Top view of the “diagonal” plot area

Figure 4.4.: Plotting regions. The cuboids corresponding to, respectively, the central coil, the windings, and the lateral coils appear colored in green, red and blue.

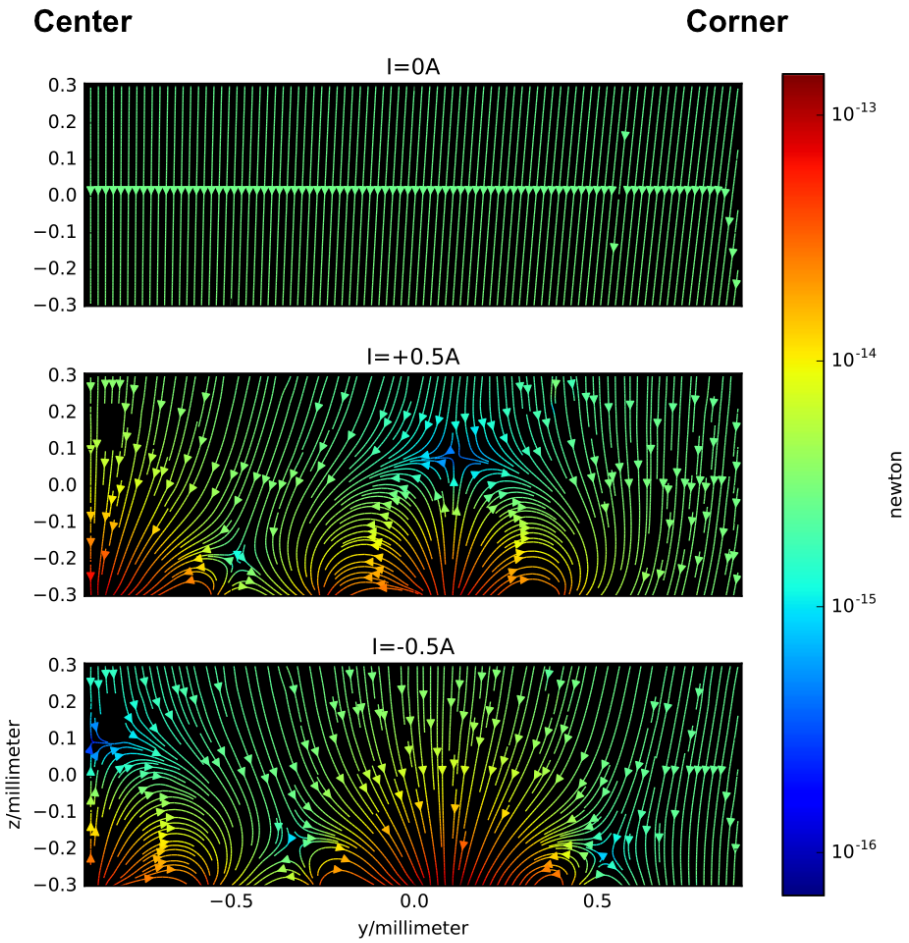

(a) Plots for the “normal” design type at the “diagonal” region. At approximately z=-0.1mm the force field moves particles between coils, but below z=-0.2mm the field moves particles between the interior and contour of each coil.

Figure 4.5.: Magnetic force field streamline plots.The y-axis is in the horizontal plane. For all regions except the “corner to edge”, its positive direction goes from the exterior to the center of the electromagnet.

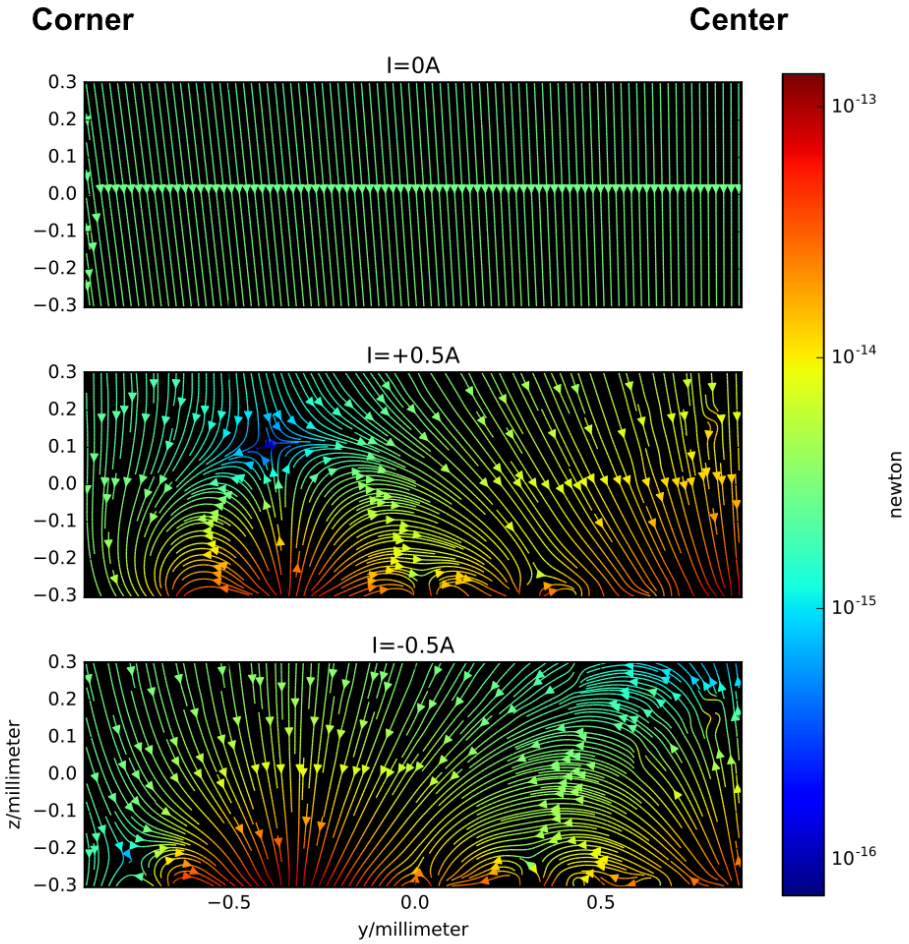

(b) Plots for the “filling close” design type at the “diagonal” region.The field becomes effective at moving particles between coils at z=-0.25mm.

Figure 4.5.

Additionally, we plotted the field near the electromagnet tracks, see figure 4.6, using $20\mu m$ as distance from the electromagnet to the bottom of the plot, and $25\mu m$ as coil height, for the “filling close” design (corresponding to figure 3.1e) .

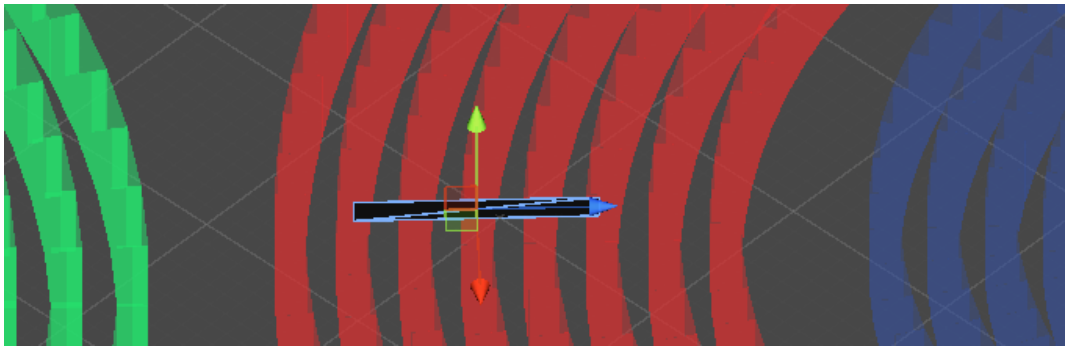

(c) Region plotted in black. The y-axis is in green, the x-axis in blue.

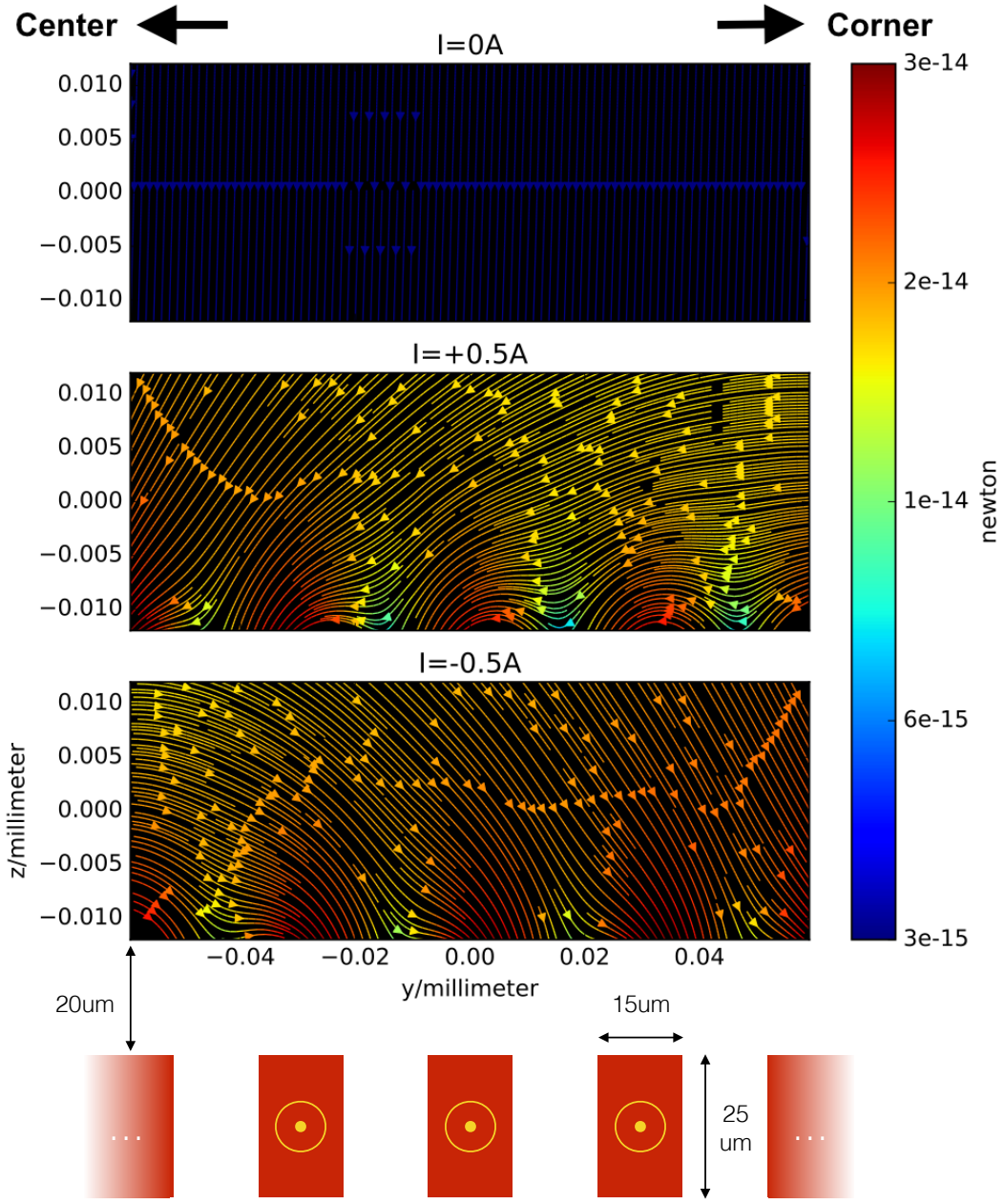

(d) Magnetic force field streamlines plot. In relation to the bottom plot, the cross section of the tracks is shown at scale and in red, and the yellow symbol marks the current positive direction, coming out of the page.

Figure 4.6.: Theoretical magnetic force results near the electromagnet tracks

4.4. Discussion

It is important to keep in mind the channel has a fixed height of 0.2mm for this analysis. From the plots in figure 4.5, for both designs presented, we can conclude that if the bottom of the channel is placed at less than roughly 100μm from the top of the electromagnet, for each coil, particles will move from the edge of the coils to the center, and vice-versa. If the channel is placed more than 0.2mm above, however, a region with low forces appears above the lateral coil, which might reduce the efficacy with which the trap moves particles.

In figure 4.6, we can see that particles sufficiently close to the bottom of the channel will be strongly pushed, relative to the rest of the force field, towards one of the sides of the current tracks, following the global pull that can be seen near the top of the plot. Sufficient separation between the channel tracks and the electromagnet will be necessary for avoiding trapping particles in these regions.

5. Magnetic Trapping Experiments

The magnetic trapping experiments were done at the microfluidics laboratory at INL under the guidance of researcher Marina Brito, among others.

5.1. Methods

Experimental Setup

The experimental setup consists of a wide-field fluorescence microscope, where the magnetic trapping device is installed, and the sources and meters associated with the electromagnet. The magnet is placed on the condenser platform of the microscope, which is not in use for fluorescence microscopy. The mechanical stage of the condenser can then be used to adjust the height of the magnet in relation to the rest of the device. A diagram can be found in figure 5.1 and photos of the setup in figure 5.2.

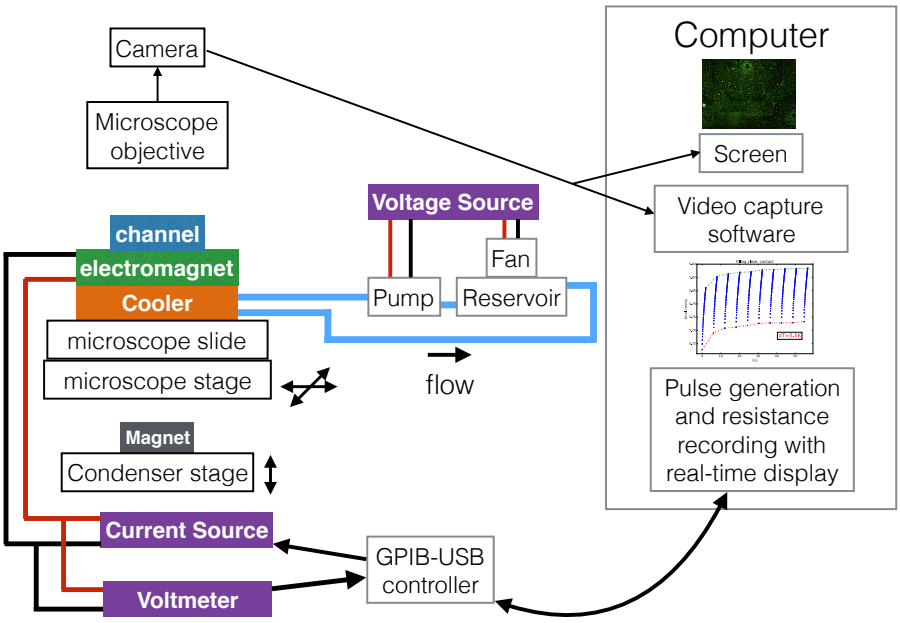

Figure 5.1.: Diagram of the experimental setup

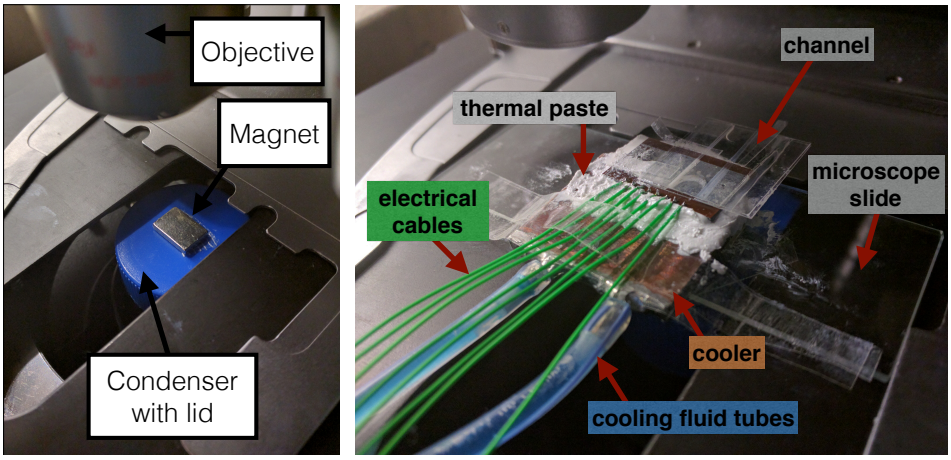

(a) permanent magnet **(b)** cooler, electromagnet and filled channel

Figure 5.2.: Device assembled under microscope. The assembly is extremely sensitive. It relies heavily on scotch tape, the thermal paste adhesive properties and is threatened by the tension imposed by the cooling system tubes.

Protocol

The channel is filled with particles; then the microscope is focused on the bottom of the channel. The magnet is brought from the lowest position to the 9mm distance from the channel. Then the electromagnet is activated, by running a sequence of 20 pulses of 2s duration and a 4s interval, with current of 0.5A. The current is inverted after the first 10 pulses. According to what is observed, the parameters can then be varied and the cycle re-run; for each sequence of pulses the microscope view is recorded.

Analysis

The videos from the experiments are interpreted visually, and compared in terms of pattern of particle displacement and speed.

5.2. Results

In this section, by an “attraction frame” we mean a video frame corresponding to a pulse that passes current counter-clockwise through the central coil, and “repulsion frame” if it goes clockwise.

In general, using the electromagnet top as the bottom of the channel resulted in particles getting stuck to the spaces matching the shape of the electromagnet tracks. This can be seen by comparing the initial state of the particles, in figure 5.4a, with their state after the electromagnet is cycled (see figure 5.4).

Inspired by the predictions of the simulation results, the second type of channel was constructed. This channel forces a separation between the electromagnet and the bottom of the channel of roughly $100\mu m$. When this channel was used, the particles stuck to channel bottom much less, and did so without forming the shape of the electromagnet tracks, as seen in figure 5.3.

When the electromagnet is turned off, zone where the particles are highly concentrated seem to relax, as seem from figure 5.3c to figure 5.3d.

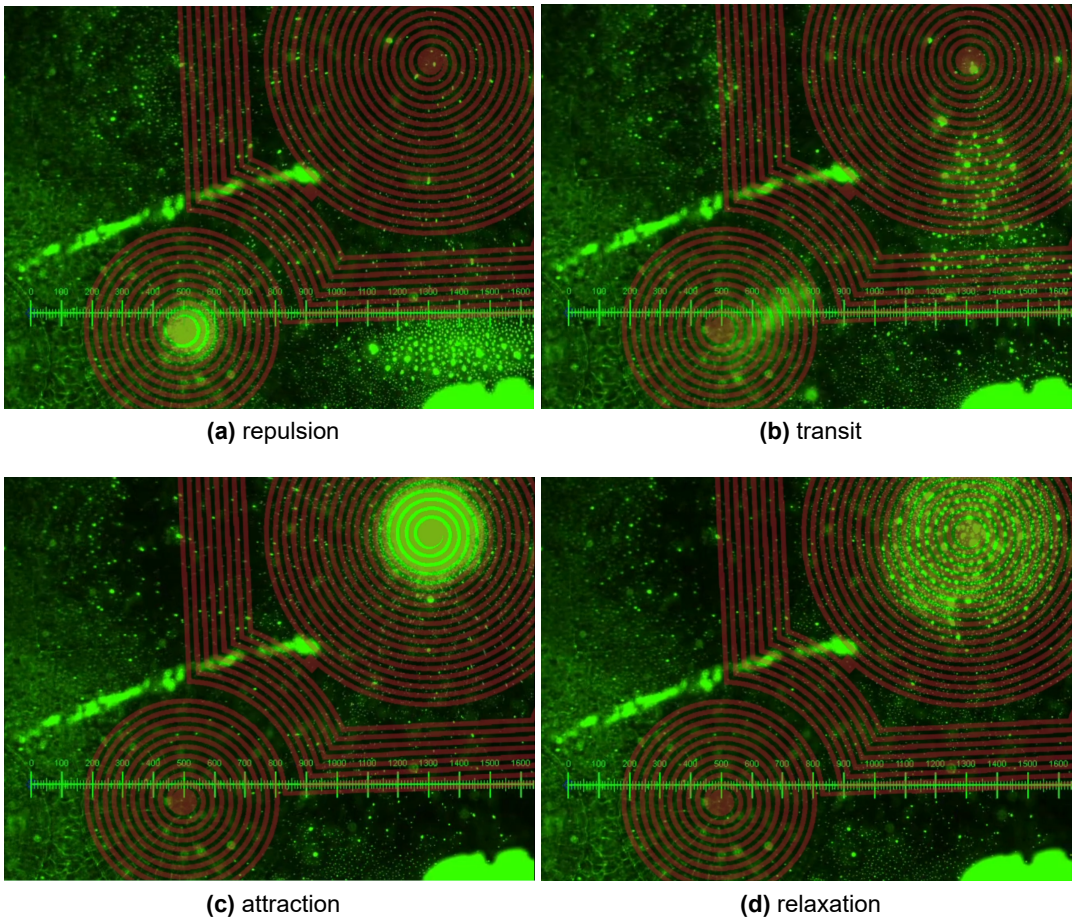

(a) repulsion **(b)** transit

(c) attraction **(d)** relaxation

Figure 5.3.: Key frames for the “filling close” design. Used 1A as current. The brown overlay is aligned with the electromagnet’s tracks. Full video here.

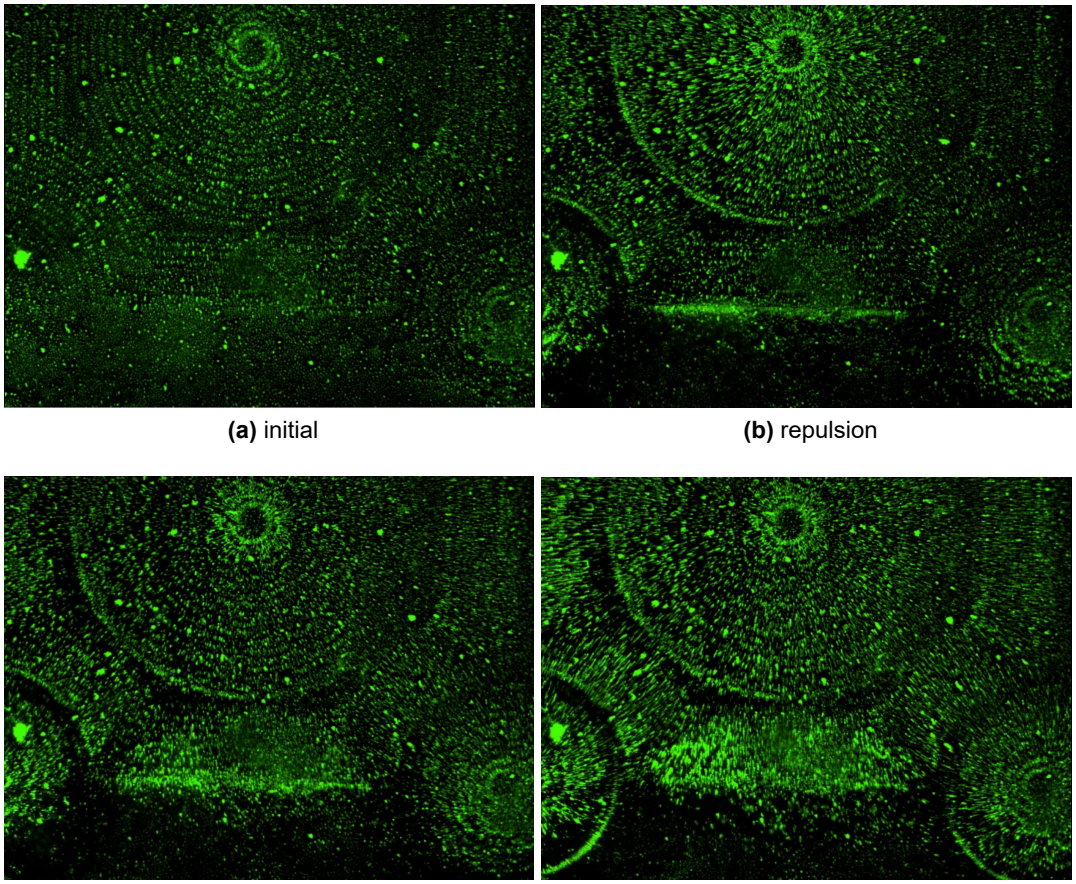

(a) initial **(b)** repulsion

(c) transit **(d)** attraction

Figure 5.4.: Frames for the “filling close” design using the electromagnet top as the channel bottom, and without the magnet in the device. Full video here.

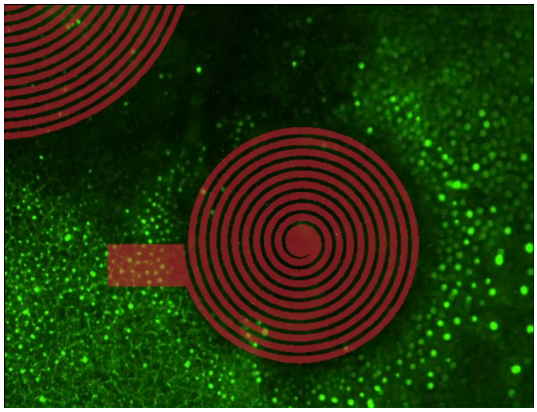

(a) attraction

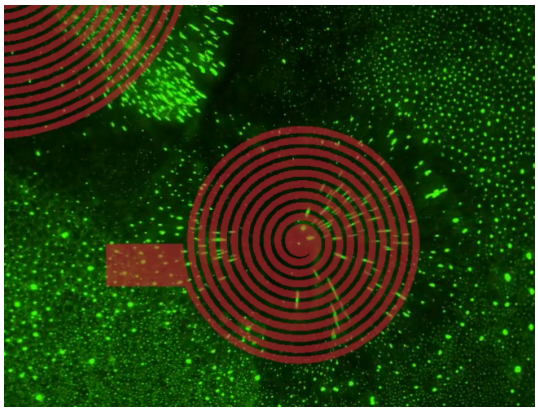

(b) transit

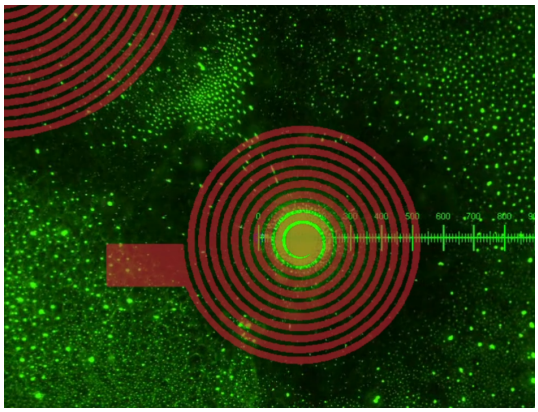

(c) repulsion

Figure 5.5.: Frames for the “large square” design using the electromagnet top as the channel bottom, and without the magnet in the device. Full video here.

Analysis

We can measure the trap effectiveness in concentrating by making the ratio between the area where particles form a high concentration disk to the area where we observe particles being pulled from. The first area can be measured by using an attraction frame after a long series of cycles. The second can be estimated by observing particle movement in the video.

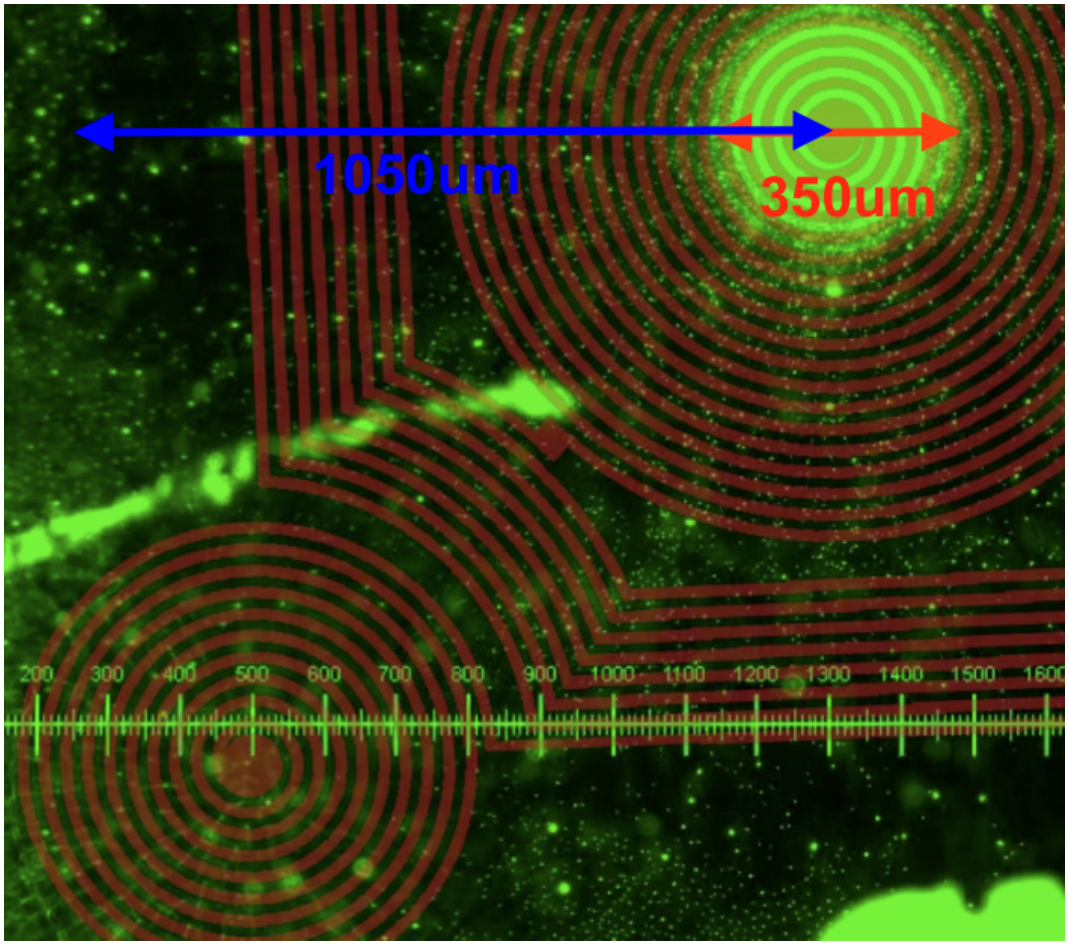

Figure 5.6.: Concentration ratio measures

From the radius in figure 5.6, we get a concentration ratio of initial area / final area $= (1050/(350/2))^2 \approx 36$.

5.3. Discussion

Generally, we observed that large amounts of particles, once brought together to the same area, agglomerate into larger diameter particulates and move faster in subsequent manipulations. When the electromagnet is turned off, large groups of these particulates disperse quickly.

Also, separating electromagnet and channel by $\approx 100\mu m$ changes the force field: particles do not stick near the tracks, and move between coils.

We note that the windings between the central and lateral coils increase coil to coil movement; more specifically, they are able to pull particles from the area between lateral coils (compare figure 5.3c with figure 5.5a).

6. Conclusion

This work created new versions of an initial magnetic trap, composed of a microfluidics channel, a permanent magnet, an electromagnet and a cooling system. New electromagnets were designed, fabricated and characterized. The construction parameters of the magnetic trap were optimized according to results of a novel simulation software. Different configurations for the device were tested in trapping experiments.

The new designs changed the number and shape of electromagnets. Their fabrication was similar to previous runs for older designs, however the copper tracks that formed the electromagnets had a non-uniform height, varying between 20 to 40 μm.

The characterization of these electromagnets included topography of the electromagnet tracks and of the final passivated surface, resistance of the each set of electromagnets and compatibility with a cooling system at set working conditions.

The characterization is being improved by magnetic field measurements at INESC-MN by Vânia Silvério. It would be interesting to compare these results to the magnetic field calculations.

The simulation software implementation is at point where interactive design of magnetic traps with instant feedback in the form of magnetic field and magnetic force field vector plots is implemented. This provided insights into the functioning of the magnetic traps, and allowed the optimization of construction parameters. Specifically, the magnetic force field matches the experimental results qualitatively. More importantly, based on the analysis of the simulation results, we increased the sep-

aration between the electromagnet and the channel to approximately $100\mu m$, and achieved effective particle movement between central and lateral coils. Future work would include particle path visualization, taking in account the pulsed nature of the electromagnet field, and interparticle interaction and agglomeration.

The trapping experiments were performed with fluorescent magnetic particles of $0.3\mu m$ of diameter, and observed via fluorescence microscopy. Via qualitative comparison, it was confirmed that trapping was improved after optimizing the trap parameters according to the simulation results. However, the experimental setup leaves much to be desired in ease of assembly and control of parameters, which makes further changes hard to systematize.

Nonetheless, we conclude that the a new design using a secondary winding around the central coil captures a larger volume of particles compared to a design without the winding; and that variations as small as $100\mu m$ between the electromagnet and the channel change drastically the trap behavior. In the future, we would like to build an easy to use configurable support for the device, and use computer aided interpretation of the capture videos to obtain displacement maps of the particles. This last item would make the analysis of the experimental results definitely objective.

For future electromagnet designs, we are interested in using the strong pull generated close to current tracks; for instance, by sequentially activating a chain of tracks, particles can be quickly moved along the bottom of a channel.

In the global view of the NANODEM project, the simulation software can be used to optimize other magnetic traps designs. However, magnetic force fields need to be compared to the adhesion forces present in the actual functionalizations of the channel surfaces, according to the desired functionality. Otherwise we might build solutions that will not work in the final product.

Bibliography

[1] Usashi Banerjee et al. “Aggregation dynamics of particles in a microchannel due to an applied magnetic field”. In: *Microfluidics and Nanofluidics* (Sept. 2012), pp. 1–13. ISSN: 1613-4982. DOI: 10.1007/s10404-012-1053-0. URL: http://dx.doi.org/10.1007/s10404-012-1053-0 (cit. on p. 3).

[2] *Bullet Physics Library*. URL: http://bulletphysics.org/ (cit. on p. 28).

[3] *C Sharp programming language*. URL: https://msdn.microsoft.com/en-us/library/kx37x362.aspx (cit. on p. 29).

[4] *COMSOL Multiphysics®*. URL: https://www.comsol.com/comsol-multiphysics (cit. on p. 28).

[5] D.C. Giancoli. *Physics: Principles with Applications*. Prentice-Hall International editions. Prentice-Hall, 1995. ISBN: 9780131834682. URL: https://books.google.pt/books?id=nCWXQAAACAAJ (cit. on p. 25).

[6] *INL- International Iberian Nanotechnology Laboratory*. URL: http://inl.int/ (cit. on pp. xiii, 1).

[7] *Instituto de Engenharia de Sistemas e Computadores - Microsistemas e Nanotecnologias*. URL: https://sites.google.com/site/inescmn/ (cit. on pp. xiv, 10).

[8] John D. Jackson. *Classical Electrodynamics Third Edition*. 3rd ed. Wiley, Aug. 1998. ISBN: 047130932X. URL: http://www.amazon.com/exec/obidos/redirect?tag=citeulike07-20%5C&path=ASIN/047130932X (cit. on p. 2).

[9] Arif Md Rashedul Kabir et al. “Drag force on micron-sized objects with different surface morphologies in a flow with a small Reynolds number”. In: *Polym J* 47.8 (Aug. 2015). Original Article, pp. 564–570. ISSN: 0032-3896. URL: http://dx.doi.org/10.1038/pj.2015.29 (cit. on p. 5).

[10] Marc Karle et al. “Controlled counter-flow motion of magnetic bead chains rolling along microchannels”. In: *Microfluidics and Nanofluidics* (Nov. 2010), pp. 1–5. DOI: 10.1007/s10404-010-0727-8. URL: http://dx.doi.org/10.1007/s10404-010-0727-8 (cit. on p. 3).

[11] *LAMMPS Molecular Dynamics Simulator*. URL: http://lammps.sandia.gov/ (cit. on p. 28).

[12] Elizabeth Mirowski et al. “Integrated microfluidic isolation platform for magnetic particle manipulation in biological systems”. In: *Applied Physics Letters* 84.10 (2004), pp. 1786–1788. DOI: http://dx.doi.org/10.1063/1.1664013. URL: http://scitation.aip.org/content/aip/journal/apl/84/10/10.1063/1.1664013 (cit. on p. 3).

[13] *NANODEM - NANOphotonic DEvice for Multiple therapeutic drug monitoring*. URL: http://nanodem.ifac.cnr.it/index.php/project-overview (cit. on pp. xiii, 1).

[14] Johan Nilsson et al. “Review of cell and particle trapping in microfluidic systems”. In: *Analytica chimica acta* 649.2 (2009), pp. 141–157. DOI: 10.1016/j.aca.2009.07.017. URL: http://www.sciencedirect.com/science/article/pii/S0003267009009222 (cit. on p. 2).

[15] Olayinka Oduwole, David Tim Grob, and Steve Sheard. “Comparison between simulation and experimentally observed interactions between two magnetic beads in a fluidic system”. In: *Journal of Magnetism and Magnetic Materials* 407 (2016), pp. 8–12. ISSN: 0304-8853. DOI: http://dx.doi.org/10.1016/j.jmmm.2016.01.043. URL: http://www.sciencedirect.com/science/article/pii/S0304885316300439 (cit. on p. 3).

[16] *Python Software Foundation*. URL: https://www.python.org/ (visited on 03/23/2017) (cit. on p. 31).

[17] Romain Ravaud and Guy Lemarquand. “Magnetic field produced by a parallelepipedic magnet of various and uniform polarization”. In: *Progress In Electromagnetics Research* 98 (2009), pp. 207–219. DOI: 10.2528/pier09091704. URL: http://dx.doi.org/10.2528/PIER09091704 (cit. on p. 3).

[18] Meritt Reynolds. “Overview of BiotSavart”. URL: http://www.ripplon.com/BiotSavart/bsov.pdf (cit. on p. 28).

[19] M. J. Rhodes. *Introduction to Particle Technology*. Chichester New York: John Wiley, 1998. ISBN: 0471984825 (cit. on p. 4).

[20] Sergey S. Shevkoplyas et al. “The force acting on a superparamagnetic bead due to an applied magnetic field”. In: *Lab Chip* 7.10 (2007), pp. 1294–1302. DOI: 10.1039/b705045c. URL: http://dx.doi.org/10.1039/b705045c (cit. on p. 5).

[21] *Super Magnet*. URL: http://supermagnet.de/ (cit. on p. 11).

[22] *Unity3D*. URL: https://unity3d.com/ (cit. on p. 29).

[23] Inc. Wolfram Research. *Mathematica*. URL: https://www.wolfram.com/mathematica (cit. on p. 68).

A. Electromagnet Fabrication

A.1. Hard Masks

For each mask, the initial substrate is a square slab of [Glass | CrO | Cr | CrO | Resist (540nm)], that is, a glass slab covered by films of, in order, from lower to superior, chrome oxide, chrome, chrome oxide, and photoresist, this last one being $540nm$ thick. The resist side is exposed by Direct Laser Writting (DWL). In a wet bench, the resist is developed, the Cr is etched, and then the resist is stripped.

A.2. Chip

In table A.1 are the substeps of the litographies performed for this fabrication sequence.

machine	process
vapor prime oven	dehydration then hexamethyldisilazane (adhesion promoter for photoresist) (HDMS) deposition
tracks	spin-coating with positive photoresist
mask aligner	exposure
microscope	visual inspection

Table A.1.: Lithography substeps.

Initial substrate The initial substrate is a Single Side Polished (SSP) Si wafer of 200mm diameter and 725μm thick.

Figure A.1.: Initial substrate

Electrical isolation Electrical isolation via deposition of $1.5\mu m$ of SiO_2.

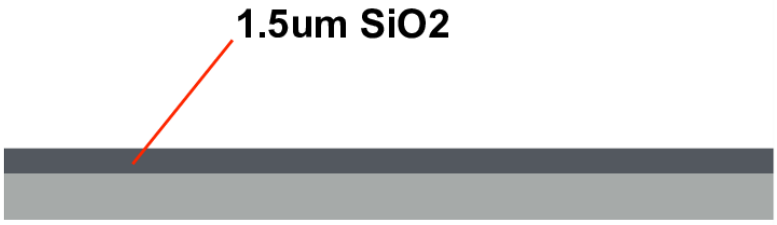

Figure A.2.: After electrical isolation

Metal sandwich / Bottom tracks Deposition of a metal sandwich of TiW(N) 15nm | Al 600nm | TiW(N) 15nm via sputtering (no temperature control, Ar and N_2 flow for TiW(N), Ar only flow for AlSiCu)

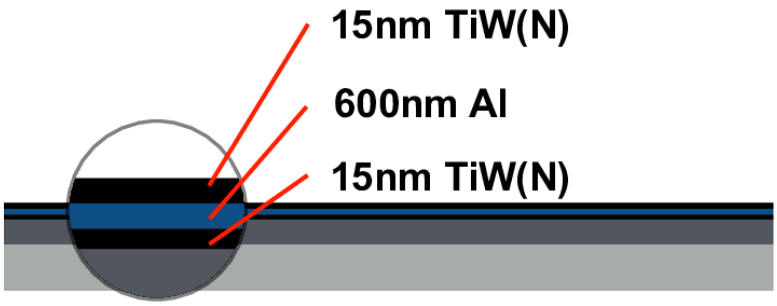

Figure A.3.: After forming bottom track

Patterning of bottom tracks

- surface treatment using O_2plasma
- litography using mask 1:metal, see substeps in table A.1
- etching of the layer of TiW(N) | Al | TiW(N), to SiO_2 layer, via Inductively Coupled Plasma (ICP) using $SiCl_4$
- resist strip via ICP using CF_4
- corrosion prevention via cleaning with De-Ionized Water (DIW)

Figure A.4.: Schematic of cross-section after patterning of bottom tracks.

Electrical isolation Electrical isolation via deposition of $500nm$ of SiO_2.

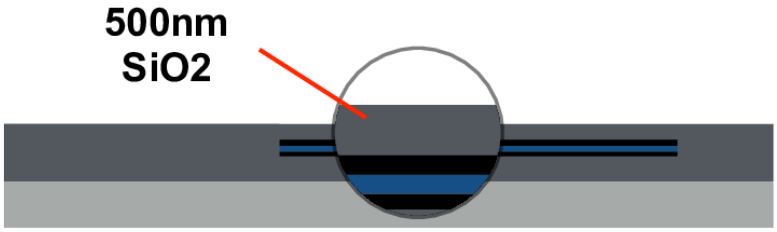

Figure A.5.: After electrical isolation

Stopping layer Deposition via sputtering of 50nm ofAl_2O_3, the stopping layer for later etch of Ta.

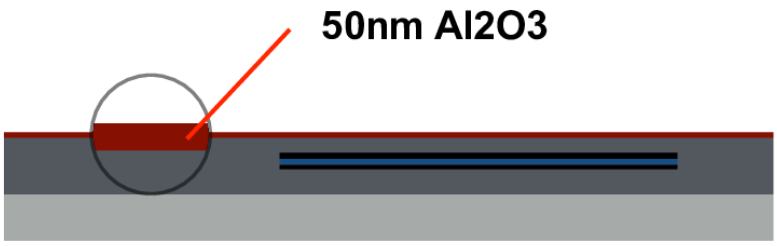

Figure A.6.: After deposition of stopping layer

Hole opening Opening of holes for connections between bottom metal and copper tracks:

- lithography using mask 2:holes, resist 1.035 µm thick, see substeps in table A.1
- etching of Al_2O_3, to SiO_2 layer, via Reactive Ion Etching (RIE)-ICP
- etching of SiO_2, to metal 1, via RIE-Advanced Plasma System (ICP-based high density plasma) (APS)

- resist strip via oxygen plasma

Figure A.7.: After hole opening

Surface cleaning Surface cleaning via Ar plasma.

Seed layer deposition Deposition via sputtering of seed layer composed of Ta 10nm | Cu 200nm for electroplating; Ta acts as adhesive for Cu.

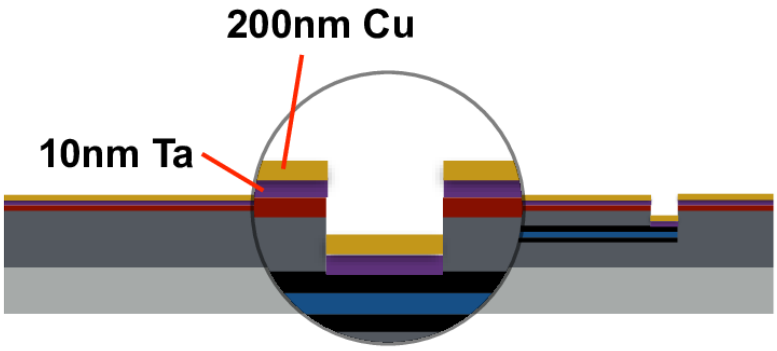

Figure A.8.: After seed layer deposition

Seed layer patterning Patterning of the exposed surface of the seed layer:

- lithography of 40μm high positive resist using mask 3:tracks, see substeps in table A.1

- descum step via oxygen plasma, for better removing exposed photoresist
- metrology of the resist heigth using a mechanical profilometer

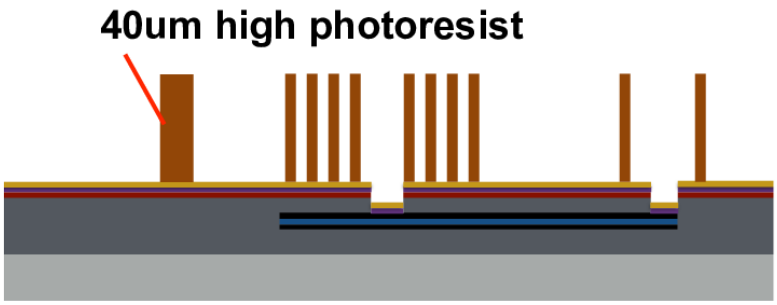

Figure A.9.: After seed layer deposition

Cu Electroplating

- Cu electroplating, with a target height of $40\mu m$, using seed layer. Duration was 280mn, at 5mA/cm^2, 24ºC,; setup was copper deposits in sulfuric acid bath, with waffer ~2/3 submerged in constant rotation at ~12rpm.
- metrology of the copper/resist heigth difference using a mechanical profilometer

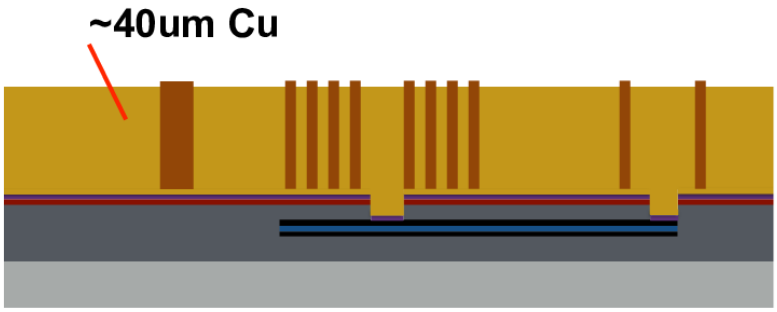

Figure A.10.: After seed layer deposition

Resist strip Wet resist strip using acetone, isopropanol, then metrology of the copper height using a mechanical profilometer.

Figure A.11.: After resist strip

Removal of seed layer

- wet etching of 200nm of Cu, using a solution of 1 part H_2O, 2 parts Al etchant
- XeF_2 dry vapor-phase etching of Ta until the Al_2O_3 layer is reached

Figure A.12.: After resist strip

Polyamide coating $20\mu m$ polyamide coating passivates, structurally reinforces and uniformizes the surface topography. This is done via spin-coating, then heating in a hot plate, then drying in an oven.

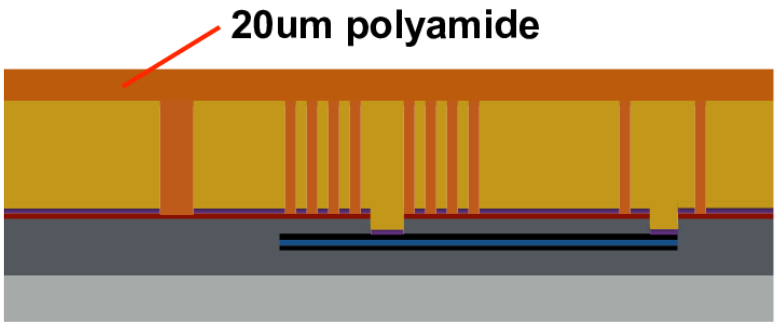

Figure A.13.: After resist strip

Cu Pads mask Deposition and patterning of a AlSiCu | TiW(N) mask over the waffer:

- deposition via sputtering of AlSiCu 1μm | TiW(N) 30nm
- lithography of 40μm high positive resist using mask 3:tracks, see substeps in table A.1
- etching of AlSiCu | TiW(N), via RIE-ICP using $SiCl_4$

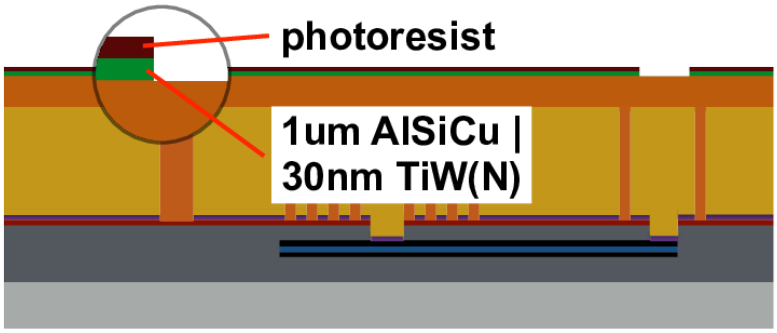

Figure A.14.: After forming pads mask

Polyamide patterning Removal of polyamide via RIE-APS using CF_4. This opens the path to the copper pads and starts digging trenches between dies.

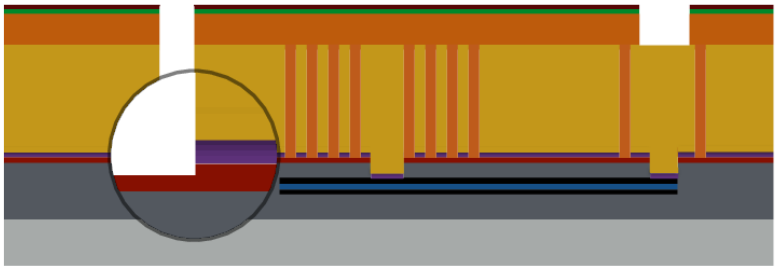

Figure A.15.: After forming pads mask

Exposing Si Etching exposes Si along die separations and holes:

- etching of Al_2O_3 via RIE-ICP
- etching of SiO_2 via RIE-APS

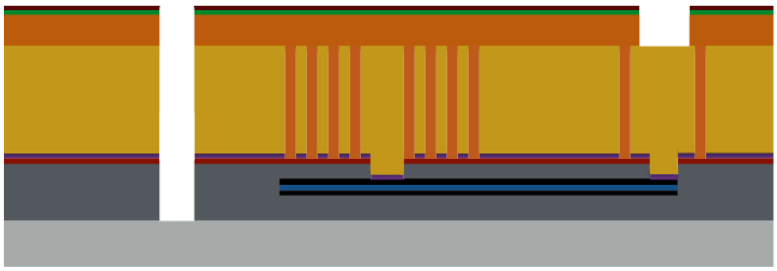

Figure A.16.: After exposing Si

Resist strip Resist strip via oxygen plasma.

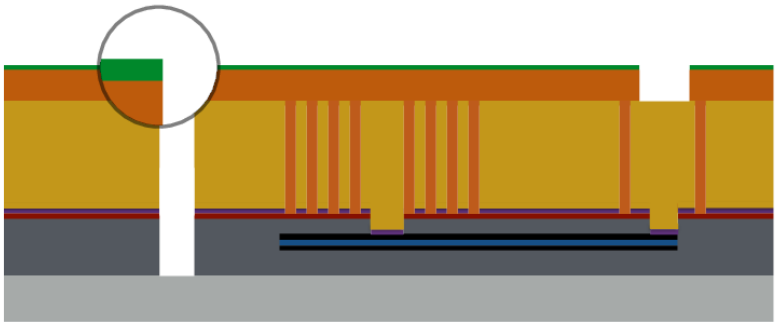

Figure A.17.: After resist strip

Si etching The waffer is mounted and glued to a support waffer. Iterative Si Direct Reactive Ion Etching (DRIE) etching with control via non-contact profilometer of trench depth separates dies and completes holes. Afterwards the dies are unglued from the support waffer and cleaned.

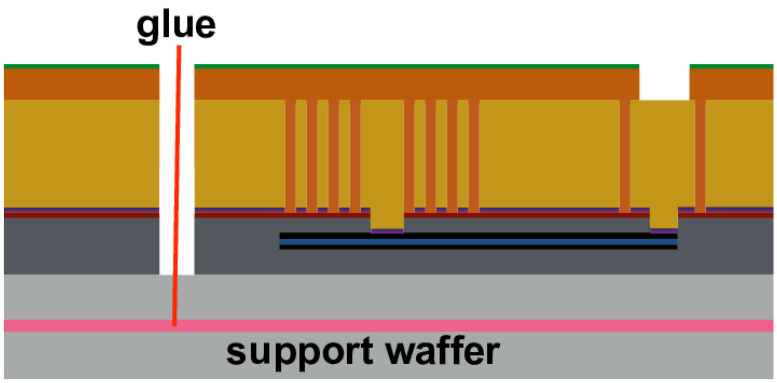

Figure A.18.: After mounting and gluing on support waffer

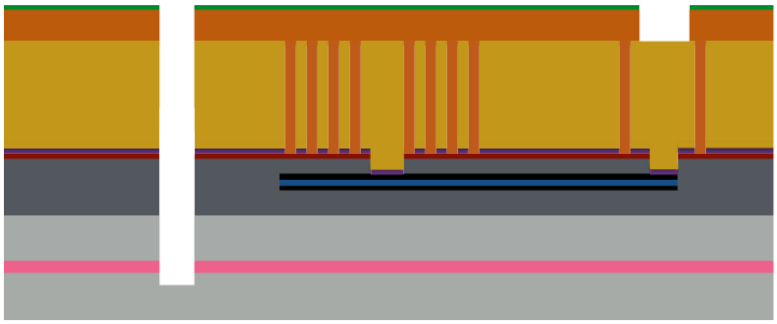

Figure A.19.: After Si etching

Removal of pads mask Removal of the AlSiCu | TiW(N) mask via wet etching of AlSiCu.

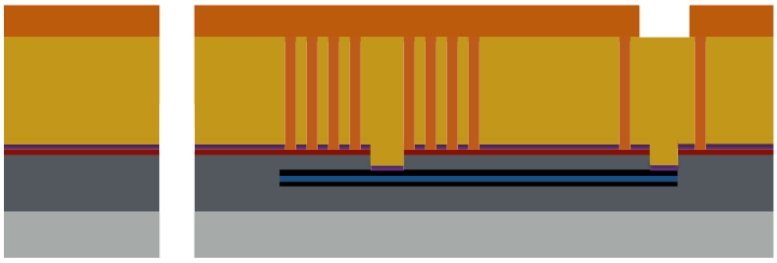

Figure A.20.: After AlSiCu etching

Reflective coating Dies are attached by kapton tape to a support waffer. Pads, holes and separations between dies are prtected by kapton tape. Then a 200nm thick AlSiCu film is deposited via sputtering (no temperature control, Ar and N_2 flow).

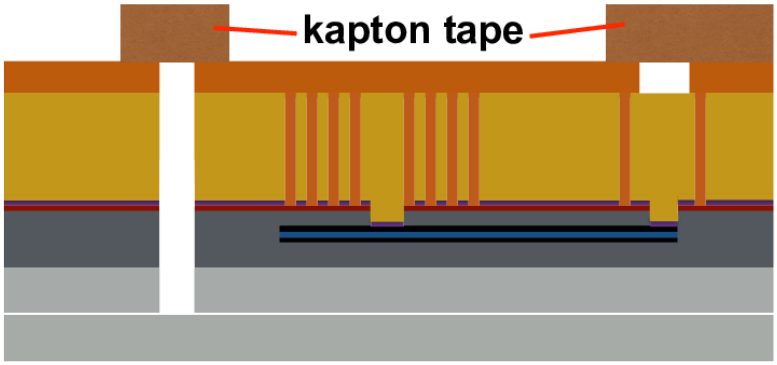

Figure A.21.: After attaching dies with kapton tape to support waffer

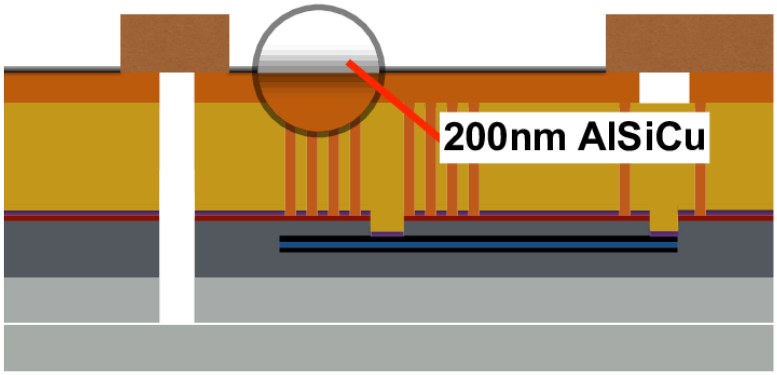

Figure A.22.: After depositing reflective film

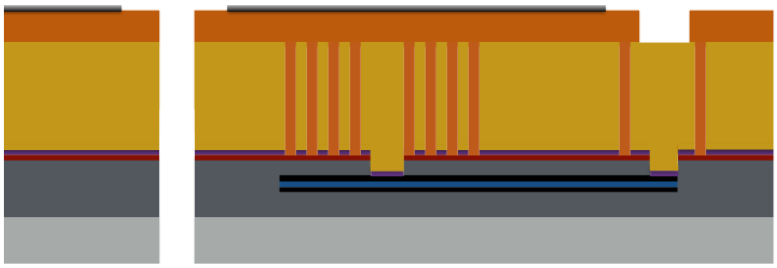

Figure A.23.: Final result

B. Mathematical derivations

Some mathematical conventions are the use of the indexes $1, 2, 3$ to indicate x, y, z. Vectors are by default in column form. More can be found in the

B.1. Magnetic force on a magnetic dipole due to a static magnetic field

In a magnetic field $\vec{B}$, given a superparamagnetic punctual dipole of moment $\vec{m} = f\left(\left|\vec{B}\right|\right)\hat{B}$, where f is define by$f(x) = V \cdot \left|\vec{M}\right|_{|\vec{B}|=x}$, then its magnetic potential $\vec{U} = -\vec{m} \cdot \vec{B} = -f\left(\left|\vec{B}\right|\right)\left|\vec{B}\right|$.

The magnetic force is then (id is a function defined by $id(x) := x$):

$$\begin{aligned}\vec{F_m} = -\nabla U &= \nabla\left((id \cdot f) \circ \left|\vec{B}\right|\right) \\ &= (id \circ f)'(\left|\vec{B}\right|) \cdot \nabla\left|\vec{B}\right| \\ &= (f + id \cdot f')(\left|\vec{B}\right|) \cdot \nabla\left|\vec{B}\right|\end{aligned}$$

We have:

$$\begin{aligned}
\nabla\left|\vec{A}\right| &= \frac{\nabla\left(\left|\vec{A}\right|\right)^2}{2\left|\vec{A}\right|} \\
\nabla\left(\vec{A}\cdot\vec{A}\right) &= \sum_{i,j}\hat{i}\partial_i\left(A_jA_j\right) \\
&= \sum_{i,j}2\hat{i}A_j\partial_iA_j \\
&= 2\left[\nabla A_j\right]\vec{A} \\
&= 2\left(\nabla\vec{A}\right)^T\vec{A} \\
&= 2\left(\nabla\vec{A}\right)\cdot\vec{A}
\end{aligned}$$

where $\nabla\vec{A} := [\partial_j A_i]$. Here $\partial_i := \frac{\partial}{\partial r_i}$ where $\vec{r} = (x, y, z)$.In some contexts this is known as the derivative of the vector $\vec{A}$.

Therefore:

$$\begin{aligned}
\nabla\left|\vec{B}\right| &= \frac{\nabla\left(\left|\vec{B}\right|^2\right)}{2\left|\vec{B}\right|} \\
&= \frac{\nabla\left(\vec{B}\cdot\vec{B}\right)}{2\left|\vec{B}\right|} \\
&= \frac{\left(\nabla\vec{B}\right)\cdot\vec{B}}{\left|\vec{B}\right|}
\end{aligned}$$

And finally:

$$\begin{aligned}\vec{F_m} &= (f + id \cdot f')(\left|\vec{B}\right|) \cdot \nabla \left|\vec{B}\right| \\ &= \left(f\left(\left|\vec{B}\right|\right) + \left|\vec{B}\right| \cdot f''\left(\left|\vec{B}\right|\right)\right) \cdot \frac{\left(\nabla\vec{B}\right) \cdot \vec{B}}{\left|\vec{B}\right|} \\ &= \nabla\vec{B} \cdot \vec{B} \cdot \left(f'\left(\left|\vec{B}\right|\right) + \frac{f\left(\left|\vec{B}\right|\right)}{\left|\vec{B}\right|}\right) \\ &= V \cdot \nabla\vec{B} \cdot \vec{B} \cdot \left(M'\left(\left|\vec{B}\right|\right) + \frac{M\left(\left|\vec{B}\right|\right)}{\left|\vec{B}\right|}\right)\end{aligned}$$

B.2. Field produced by cuboid of uniform current density

In this section we derive an expression for the magnetic field $\vec{B}$ at a point $\vec{r_o}$ produced by a cuboid, i.e. a parallelepiped of straight angles, of length a, width b and height, through which passes a uniform current density $\vec{J}$. Let $\vec{s} := (a, b, c)$. We place the cuboid so that it has two of its 8 corners at $\vec{s}/2$ and $-\vec{s}/2$. From Bio-Savart's formula (equation (1.2)), we obtain:

$$\vec{B} = \frac{\mu_0}{4\pi}\vec{J} \times \int_{-a/2}^{a/2}\int_{-b/2}^{b/2}\int_{-c/2}^{c/2}\left(\frac{\vec{r'}}{|\vec{r'}|^3}dx'dy'dz'\right) \tag{B.1}$$

Where $\vec{r'} = \vec{r_o} - \vec{r}$ and $\vec{r} = (x, y, z)$. Let $\vec{U}$ be the right factor of the cross-product.We used the symbolic calculation software Mathematica[23] for obtaining the indefinite integral $\vec{u}(x, y, z) = \iiint \frac{\vec{r}}{|\vec{r}|^3}dV$ in closed form. Therefore we can write $\vec{U} = \vartheta\vec{u}$, where:

$$\vartheta f := -\sum_{i=1}^{2}\sum_{j=1}^{2}\sum_{k=1}^{2}(-1)^{i+j+k}\left(f|_{x\leftarrow x_o-(-1)^i a/2, y\leftarrow y_o-(-1)^j b/2, z\leftarrow z_o-(-1)^k c/2}\right)$$

where $a \leftarrow b$ indicates symbolic replacement of a by b, $(x_o, y_o, z_o) := \vec{r}_o$, and the leading minus is required by the change of variable from $\vec{r'}$ to $\vec{r} = \vec{r_o} - \vec{r'}$.

Let P_S be the operator that permutes the symbols $\{x, y, z\}$ according to a permutation S of 3 elements. Let S_i be the cyclic permutation of x, y, z that map x to r_i. By symmetry, we have $\vartheta \vec{u}_i = \vartheta P_{S_i} \vec{u}_1$.

Any term in $\vec{u}$ that depends only on two of the variables x, y, z is nulled by the summation performed by ϑ; after removing those terms from what Mathematica yields, we can use $\vec{u} = Ph$, where h is a scalar expression in x, y, z, and P is an operator defined by $Pf = (P_{S_1} f, P_{S_2} f, P_{S_3} f)$, i.e. it takes an expression and constructs a 3-vector by cyclically permuting x, y, z.

Calculating the gradient yields:

$$\nabla \vec{B} = [\partial_j B_i] = \left[\partial_j \vec{B}\right] = \left[\frac{\mu_0}{4\pi} \vec{J} \times \partial_j \vec{U}\right] := \frac{\mu_0}{4\pi} \vec{J} \times \left[\partial_j \vec{U}\right]$$

where we defined the cross-product of a vector by a matrix as $\vec{a} \times M := [\vec{a} \times col_j M]$.

We have $\left[\partial_j \vec{U}\right] = [\partial_j \vartheta \vec{u}] = \vartheta [\partial_j \vec{u}] = \vartheta [\partial_j P h] = \vartheta [\partial_j P_{S_i} h] = \vartheta \left[P_{S_i} \partial_{S_i^{-1}(j)} h\right] = \vartheta \left[P_{S_i} (\nabla h)_{S_i^{-1}(j)}\right]$. We calculate ∇h, and eliminate terms with only two variables as we did for $\vec{u}$, obtaining $\vec{g}$.

Both h and $\vec{g}$ can be written in terms of $n := |\vec{r}|$, $\vec{w} := P\, arctan(\frac{yz}{xn})$, $\vec{l} := P\, ln(x+n)$. Then:

$$\vec{g} = (w_x, -l_z, -l_y), \quad h = \vec{r} \cdot \vec{g}$$

Therefore:

$$\left[P_{S_i}\vec{g}_{S_i^{-1}(j)}\right] = \begin{bmatrix} w_x & -l_z & -l_y \\ -l_z & w_y & -l_x \\ -l_y & -l_x & w_z \end{bmatrix} =: G(\vec{w},\vec{l})$$

So G is linear in $\vec{w}$ and $\vec{l}$. Therefore $\left[\partial_j\vec{U}\right] = \vartheta P\left(\vec{g}^T\right) = \vartheta G(\vec{w},\vec{l}) = G\left(\vartheta\vec{w},\vartheta\vec{l}\right)$ and we have:

$$\vec{B} = \frac{\mu_0}{4\pi}\vec{J}\times\vartheta P\left(\vec{r}\cdot\vec{g}\right), \quad \nabla\vec{B} = \frac{\mu_0}{4\pi}\vec{J}\times G\left(\vartheta\vec{w},\vartheta\vec{l}\right)$$

Identifying these patterns helped to build efficient code for the calculation of both the field and its gradient. Their derivation can be found in this linked MATHEMATICA notebook.

C. Implementation details

C.1. Pseudo-code for the field of a cuboid conductor

In these calculations, the current I going through the cuboid is known, and the current density is assumed to be uniform and points to $\hat{x}$, so$\vec{J} = \frac{I}{bc}\hat{x}$ .Pseudo-code for its evaluation can be found in C.1.

Its correctness requires some justification and assumes some limitations. $\vec{r_o}$ is assumed to be at least a small ϵ away from the cuboid, so, for each corner in the summation performed by ϑ, at least one of the x, y, z will not be zero.

The expression for $\vec{w}_i$ is not defined at $r_i = 0$; the implementation however interprets $1/0$ as $+\infty$, and defines $atan$ correctly for that limit . We know the correct value can be given by taking the limit $r_i \to 0$. The approach sign (e.g. positive through $r_i \to 0^+$) is the same for each four corners that have $r_i = 0$. E.g. for $r_i = x$, those 4 corners would be either at $x_o = a$ or $x_o = -a$. Since the summation performed by ϑ will null these terms of equal modulus but different signs, the correct result is zero; the implementation gives the correct result since the default value is constant.

For h, in doing the limit, the right factor w_x in the term $x \cdot w_x$ is bounded and the left one tends to zero; so the correct value is zero. In the implementation, w_x is also bounded and x is zero, so the same result is obtained.

$\vec{l_i}$is not defined for $r_i = -n \Leftrightarrow (r_i \leq 0 \& (\forall j \neq i : r_j = 0))$, i.e., the lines parallel to the axes going from the corners of the cuboid to the negative cartesian directions . Under the previous assumptions, for a fixed $\vec{r_o}$ this happens for a single index i

at a single corner. From equation (B.1) we have $\vec{B}(\vec{r}) = -\vec{B}(-\vec{r})$, and therefore $\nabla\vec{B}(\vec{r}) = [\partial_j(-B_i(-\vec{r}))] = [(\partial_j B_i)(-\vec{r})] = \nabla\vec{B}(-\vec{r})$. Therefore we can calculate at $-\vec{r_o}$, changing the sign of r_i and thus avoiding indeterminations. In practice we perform this transformation each time $\forall i : (\vec{r_o} - (1+\epsilon)\vec{s})_i < 0$ for a positive ϵ; for the calculations presented in this thesis we used $\epsilon = 0.1$. This epsilon reduces numerical error. This condition describes an infinite volume delimited by three orthogonal planes parallel to the faces of the cuboid with normals $\hat{x}, \hat{y}, \hat{z}$.

Algorithm C.1 Pseudo-code for the field and correspoding gradient of a cuboid of uniform current density, with most operators expanded.

input $I, (a, b, c), \vec{r_o}$
output $\vec{B}, \nabla\vec{B}$
$\vec{J} := \frac{I}{bc}(1, 0, 0)$
if $(\vec{r_o} - (1 + \epsilon)\vec{s}) \in (\mathbb{R}^-)^3$ then **then**
  $s := -1$
else
  $s := 1$
end if
$\vec{r_d} := s \cdot \vec{r_o}$
$\vec{H} := \vec{0}$
$\vec{W} := \vec{0}$
$\vec{L} := \vec{0}$
$i := 0$
for $i < 2$ **do**
  $j := 0$
  for $j < 2$ **do**
    $k := 0$
    for $k < 2$ **do**
      $\vec{r} := (x, y, z) = \vec{r_d} - \left((-1)^i a/2, (-1)^j b/2, (-1)^k c/2\right)$
      $n := |\vec{r}|$
      $sgn := -(-1)^{i+j+k}$
      $\vec{w} := (atan(\frac{yz}{xn}), atan(\frac{zx}{yn}), atan(\frac{xy}{zn}))$
      $\vec{l} := (ln(x + n), ln(y + n), ln(z + n))$
      $\vec{h} := (xw_x - yl_z - zl_y, yw_y - zl_x - xl_z, zw_z - xl_y - yl_x)$
      $\vec{H} := \vec{H} + sgn \cdot \vec{h}$
      $\vec{W} := \vec{W} + sgn \cdot \vec{w}$
      $\vec{L} := \vec{L} + sgn \cdot \vec{l}$
      $k := k + 1$
    end for
    $j := j + 1$
  end for
  $i := i + 1$
end for
$\vec{B} := \frac{\mu_0}{4\pi}\vec{J} \times \vec{H} \cdot s$
$$\nabla\vec{B} := \frac{\mu_0}{4\pi}\left[\vec{J} \times \begin{bmatrix} W_x \\ -L_z \\ -L_y \end{bmatrix}, \quad \vec{J} \times \begin{bmatrix} -L_z \\ W_y \\ -L_x \end{bmatrix}, \quad \vec{J} \times \begin{bmatrix} -L_y \\ -L_x \\ W_z \end{bmatrix}\right]$$